LABORATORY OF NUCLEAR MEDICINE AND RADIATION BIOLOGY

900 VETERAN AVENUE

UNIVERSITY OF CALIFORNIA, LOS ANGELES, CALIFORNIA 90024

AND DEPARTMENT OF RADIOLOGY

UCLA SCHOOL OF MEDICINE, LOS ANGELES, CALIFORNIA 90024

This work was partially supported by ERDA Contract #EY-76-C-03-0012 and NIH grant 7-R01-GM-24839-01.

Prepared for U.S. Energy Research
and Development Administration
under Contract #EY-76-C-03-0012

ECAT: A New Computerized Tomographic Imaging System for Positron-Emitting Radiopharmaceuticals

Michael E. Phelps, Edward J. Hoffman
Sung-Cheng Huang and David E. Kuhl

DISCLAIMER

ECAT: A NEW COMPUTERIZED TOMOGRAPHIC IMAGING SYSTEM FOR POSITRON-EMITTING RADIOPHARMACEUTICALS

Michael E. Phelps, Edward J. Hoffman, Sung-Cheng Huang and David E. Kuhl

Center for the Health Sciences

and

Laboratory of Nuclear Medicine and Radiation Biology
University of California, Los Angeles
Los Angeles, California 90024

For reprints contact: Michael E. Phelps
Division of Nuclear Medicine
Center for the Health Sciences
University of California, Los Angeles
Los Angeles, California 90024

This work was partially supported by ERDA contract EY-76-C-03-0012 GEN-12, NIH grant 7Ro1-GM 24839-01.

ABSTRACT

The ECAT was designed and developed as a complete positron imaging system capable of providing high contrast, high resolution, quantitative images in 2 dimensional and tomographic formats. Flexability, in its various image mode options allow it to be used for a wide variety of imaging problems. High (HR), medium (MR) and low (LR) tomographic resolution is 0.95 ± 0.1, 1.3 ± 0.1 and 1.7 ± 0.1 cm FWHM; high, medium and low resolution in 2-D images are 0.85 ± 0.1, 1.3 ± 0.1 and 1.7 ± 0.1 without or with some variation in depth depending on resolution mode employed. ECT system efficiency is 30,100, 15,900 and 9,200 c/sec/μCi/cc with a 20 cm diam phantom at LR, MR and HR. Due to geometric,detector, electronic and shielding design, countrate capability and linearity are high with minimum detection of scattered radiation and random coincidence. Measured error was found to be in excellent agreement with theoretical statistical predictions down to a level of 1.4% standard deviation. Redundant sampling scheme of ECAT is shown to significantly reduce errors due to motion and detector instability. Scan times are variable from 10 sec to multiple min/slice in which multiple levels are automatically carried out by computer control of patient bed. A wide variety of animal and human studies illustrate image quality, resolution and efficiency of both ECT and 2-D imaging mode. These studies also provide examples of the non-invasive study method which has been made possible through development of ECT. Unique potential of this developing modality (*Physiologic Tomography*) can provide important information not obtainable from the primarily morphologically oriented techniques of x-ray CT and ultrasound.

A number of different emission computerized tomographs (ECT) have been or are being developed at this time. These systems employ a wide range of design concepts and are in various stages of application, development or design. These systems can be generally categorized as either single photon counting (SPC) systems which employ the principles of either scanners, or scintillation cameras to the technique of reconstruction tomography for the imaging of compounds labeled with ^{99m}Tc, ^{201}Tl, ^{123}I, ^{131}I, etc. This approach is exemplified with the multiple detector array designs of Kuhl et al. (1,2), Mallard et al. (3) J & P Engineering[1] and Union Carbide[2] and with the scintillation camera approach of Keyes et al. (4), Budinger et al. (5,6) and Jasczak et al. (7). The second approach employs the use of annihilation coincidence detection (ACD) for the imaging of positron emitting radiopharmaceuticals. The ACD approach is exemplified by the single slice multiple detector hexagonal designs of Phelps, Hoffman Ter Pogossian et al. (8-11), the multi-slice, multi-detector hexagonal design of Ter Pogossian, Mullani, Higgins et al. (12), the multiple crystal dual headed camera approach of Brownell et al. (13,14), the dual headed scintillation camera approach of Muehllenher, Harper et al. (15,16), the dual headed multi-wire proportional chamber approach of Kaufman, Perez-Mendez et al. (17,18), and the circular ring systems of Robertson et al. (19), Yamamoto et al. (20), Cho et al. (21,22) and Derenzo, Budinger et al. (23,24).

A new positron tomograph, ECAT, was designed by two of the authors (MP & EH), prior to coming to UCLA, build by ORTEC[3] and was delivered to UCLA in January 1977. We have tested and are now routinely carrying out studies with this system. The ECAT was specifically designed to produce transaxial tomographic images of the distribution of positron-emitting radiopharmaceuticals in any portion of the human body. It is also capable of producing quantitative 2-dimensional images.

---

[1] J & P Engineering, England
[2] Union Carbide Imaging Systems, Norwood, Massachusetts (formally Clean Corp.)
[3] ORTEC, Inc., Oak Ridge, Tennessee

While the ECAT embodies many of the basic principles and design concepts developed in PETT III (8-10, 25) it has been redesigned and optimized in terms of the physical design and inherent imaging characteristics. The ECAT has been designed to be a complete imaging system allowing a great deal of flexibility in its various imaging modes so as to handle a variety of imaging problems.

This paper presents: (i) a description of the ECAT; (ii) phantom studies to illustrate the systems resolution, efficiency, linearity, accuracy, field uniformity and design approach which minimizes the acceptance of random coincidence and scattered radiation; and (iii) representative studies in animals and patients in both the transaxial tomographic and 2-dimensional imaging modes.

ECAT DESIGN CRITERIA

The design objective of the ECAT was to develop a complete positron imaging system capable of providing not only transaxial tomographic images but also conventional 2-D images for greater flexibility and utility. A great deal of effort was expended in developing a truly quantitative instrument since the greatest strength of emission computed tomography (ECT) is in quantitatively measuring physiologic processes (26-28). From strictly an imaging point of view, the quantitative imaging capability will also provide maximum image contrast. With these general objectives in mind the following criteria was used as guidelines in developing the ECAT.

(i) flexible sampling capability in both the linear and angular direction consistent with;

(a) reconstructed image resolution (ie, sampling distance $\leq$ ½ image resolution)

b) inherent detector resolution (ie, sampling distance $\leq$ ½ inherent detector resolution)

c) required image accuracy (ie, no sampling artifacts)

ii) Accurate method for photon attenuation correction

iii) Uniform detector resolution and sensitivity with depth

iv) Minimum detection of scattered radiation and random coincidence events

v) High sensitivity to meet the demanding statistical requirements of CT and to minimize scan times

vi) Linear response of detectors over count rates encountered

vii) High count rate capability

viii) Accurate mechanical positioning resolution (ie, no artifacts due to mechanical detector positioning)

ix) Both 2-D and 3-D imaging capability.

x) User oriented system operation.

The importance of each of these factors has been discussed previously in the design of ECT systems (8,9,27-30). The importance of providing a conventional 2-D imaging capability with an ECT system has been previously discussed by Keyes et al. (4). While we agree with the importance of the 2-D imaging capability as discussed by Keyes et al., it was also felt that the ECAT should not only provide a stand-alone 2-D imaging capability but that the 2-D image would improve both the accuracy and efficiency of the use of the tomographic mode. For instance, rapid 2-D images taken with the ECAT are used interactively to select levels to be studied in more detail with the ECT mode. This interactive mode is used both with emission and transmission techniques to facilitate set-up of

patients for ECT studies.

Another design choice was in the area of single slice versus multiple slice capabilities. A factor in this aspect was a cost-design decision in an effort to maintain a realistic system cost without sacrificing imaging capabilities. However, there are also fundamental factors which relate to single slice versus multiple slice designs which are the following:

i) The first priority in the design approach to the ECAT was to produce quantitative, high contrast transaxial tomographic images of highest quality. This strongly dictates that the maximum detection efficiency be placed in a plane circumferential to the patient to optimize efficiency in this mode.

ii) Maximum signal to noise ratios and quantitative accuracy can be obtained by reducing the singles count rate (ie, random coincidence rate) and true coincidence due to scattered radiation by employing slit shields of sufficient thickness and length and minimum open area to restrict the radiation accepted by each detector to the examined plane (8,31) (ie, reduction of singles count rate and scattered coincidence from activity above and below the plane of interest). The magnitude of the importance of the slit shields can be appreciated from the analytical work of Derenzo et al. (23) which showed that the random coincidence rate and coincidence scatter detection rate increased in proportion to the height of the slit opening to the fourth and third power, respectively. Lead shielding around the detectors further reduces singles count rate and detector-to-detector scatter coincidence.

iii) Since the data used to reconstruct a single transaxial plane are inter-

dependent it is important to place the maximum efficiency in the circumferential configuration to collect rapidly these data before patient motion, organ motion or activity movement occur which cause inconsistencies (ie, distortions) among these interdependent data. For example, consider a single slice (ie, a system which takes multiple slices serially one at a time) and a five slice system in which both systems have the same total detection efficiency (ie, the five slice system has 1/5 the efficiency per slice of the single slice system). These two systems could collect data for five slices in the same total time. However, the single slice system would spend one-fifth of the time collecting the interdependent data for each transaxial image. From this point of view, the single slice system would be fundamentally preferred since any movement that occurred during the data collection of one plane in a single slice system does not affect the other planes due to the independence of one plane to another. Any motion that occurred during the total scan time of the five slice system would effect all five slices.

ECAT

The ECAT system (Fig. 1) is based on optimized design criteria from experience gained in the development of the PETT II and III positron transaxial tomographs (8-10, 25, 31). The ECAT consists of a hexagonal array of sixty six 3.8 x 7.5 cm NaI (T1) detectors in which all detectors on opposing banks are coupled electronically in a multiple coincidence format (Fig. 2). The 11 detectors on each opposing bank produce 121 lines of coincidence response for each detector bank pair or a total of 363 lines of response for the total system. The coincidence time resolution for the system is 20 nanoseconds. The distance between opposing banks of the detectors is 100 cm and the total field of view of the system is a circle with a 50 cm diameter.

The placement of the 66 detectors with respect to one another, the inner bank separation distance and detector size are interrelated factors which must be correctly matched for optimum image reconstruction. The detailed relationships between these factors have been discussed in detail elsewhere for the PETT III (9,10,25,30). Even though the individual parameters in the ECAT differ from the PETT III, the general relationships and requirements discussed in the above references apply to the ECAT.

The lead shielding, critical for optimal and quantitative performance, is designed to protect the detectors from radiation originating in parts of the body outside the fields of view. This reduces the loss of resolution and contrast which arises from accidental or random coincidences and those true coincidences due to scattered radiation. This also allows high count rate capability to be achieved since the above factors are rate limiting in positron systems. Most of the lead shielding is provided by two stationary lead discs (1.5" thick) which are placed on either side of the plane of interest. These shielding discs extend from beyond the NaI (Tl) detectors in towards the center to a 60 cm diameter at the center. The detectors are embedded in lead blocks which act not only as detector holders, but provide additional lead shielding to reduce detector-to-detector scattering to a value of about 0.5% of the true coincidence counting rate. Thin lead shielding (1.6 mm) is also provided on the inside of the plastic covers of the gantry to reduce the low energy radiation (ie, < 300 KeV) from the patient which scatters from different parts of the tomograph and from the walls of the imaging room.

Since the exposed detector diameter defines the inherent spatial resolution, the ECAT resolution is varied by placing a lead shadow shield in front of each bank of detectors with an opening consistent with the desired spatial

resolution. Currently, the shadow shields used on the ECAT consist of rectangular holes that are flared at different angles to allow each detector an unobstructed view of all the detectors on the opposing bank. The width of the holes in the two types of shadow shields presently used are either 2.3 or 1.5 cm wide by 3.8 cm in the axial direction. These shadow shields produce an average detector pair resolution of about 1.1 and 0.8 cm full width half maximum (FWHM), respectively in the plane. The resolution in the axial direction for both of the slit shields is about 1.9 cm. With the 3.8 cm diameter NaI (Tl) detector fully exposed (ie, no shadow shields) the average detector pair resolution is about 1.6 cm in the plane and about 1.8 cm in the axial direction. Removable covers are provided on the front of the ECAT gantry for insertion or removal of the shadow shields (Fig. 1). The six shadow shields for the six banks of the detectors require several minutes to change.

The output of the detectors is amplified by a factor of 10 through a fast preamplifier. The signal is then sent to a discriminator which provides energy discrimination (typically a 100 KeV threshold) and converts the analog detector pulse to a logic pulse for timing. The logic pulses from all eleven detectors in each bank are routed to a mixer which provides a single output signal. The output signals from the mixers from two opposing detector banks are routed to a coincidence unit. This coincidence unit establishes the occurrence of coincidences between all pairs of opposing detectors. The actual detector pair in which a coincidence has occurred is identified by using the output of the coincidence unit to strobe open a set of 11-one bit latches that are connected to the detectors on a bank. When a coincidence occurs, bits are set for the two detectors in which the events originated. These bits are a binary word. This 22 bit binary word is then

encoded into a 9 bit word which is transferred to a buffer memory and finally to the computer. This design reduces cost and complexity since it only requires three coincidence circuits, three binary coding modules and one encoding module to establish the total 363 coincidence combinations of the system.

All of the electronics for the ECAT are in modular form, either NIM[3] or CAMAC[3]. The discriminators, coincidence circuits and mixer are NIM modules while the encoders, buffer memories, a real-time clock, stepping motor controllers for the gantry and bed, and the interface between the scanner and the computer system are in CAMAC.

The computer system of the ECAT performs many operations such as control of (i) the linear and angular scanning motion of the gantry and the linear motion of the patient bed, (ii) data collection, sorting, attenuation corrections and reconstruction of the image. (iii) data display and processing of data with region of interest (ROI), histogram, and grey (and color) scale windowing capabilities via a joy stick. (iv) hard copy output of data through a line printer/plotter and (v) long term storage of information on floppy discs. All of the operations of the ECAT, although controlled through the computer, are accessed by the user through a simple question and answer format with the video terminal of the control console (Fig. 1). The initiation of the system operations are provided through push-buttons on the control console (ie, normalize,scan, attenuation correct, display, histogram, region of interest, grey scale windowing, pause, reset, abort, etc.).

The basic configuration of the ECAT is shown in figure 3 which illustrates the functional aspects of the system. Data are displayed with a memory buffered

---

[3]NIM is an industry standard for Nuclear Instrument Modules. CAMAC is an industry standard for Computer Aided Measurement And Control.

video display system in a 256 x 320 format with 64 grey or color scales. A small display is used for photographing with either polaroid or 8" x 10" transparency while two large displays (Blk/wht and color) are used for viewing and photographing. Images can be displayed and photographed in a single or multiple image format. A joy stick is employed to outline regions of interest for automatic calculation of area and mean ± std. deviation of image values (See Fig. 6) and to display data within a selected grey scale range or window. A triple-drive double-sided floppy disc with 1.87 mega bytes of storage is used for patient data. A 7.5 mega byte fixed and removable disc is used for high speed bulk storage and a printer/plotter provides a hard copy. The computer is a PDP 11/45 with 32 K of memory.

The bed of the ECAT can be raised from a level of 30" to 38" above the floor or moved in and out of the tomograph for patient positioning by manual control buttons on the side of the bed. A low power neon laser is used to illuminate a narrow line across the subject in the detector plane for convenient set up and identification of scan positions. The bed can also be moved from the control console by the user with the joy stick or under program control.

Cardiac gating is provided by partitioning the CAMAC buffer memory into sections for data collected during different phases of the cardiac cycle. The selected phase is identified with the ECG gating unit which provides a routing signal to store the data in proper sections of the CAMAC buffer memory. These data are then transferred to the computer for reconstruction of the cross sectional images of each selected phase of the cardiac cycle.

Non uniformity in efficiency between detectors is removed by routinely calibrating the system with a plane source which mounts on tracts in the center cover. Initially this calibration was run daily but long term stability of the system has shown that a weekly calibration is more than adequate,

RECTILINEAR SCAN MODE

Rectilinear scans are performed by a combination of linear scans of detector banks followed by discrete movement of the patient bed in the axial direction (gantry is not rotated). The typical sampling resolution is 5.7 mm and 6 mm in the transverse and axial direction, respectively. Three views (ie, from the 3 opposing detector banks) are simultaneously recorded and displayed; an anterior-posterior and two obliques at ± 60°. The collected data are sorted and displayed in high (HR), medium (MR) or low (LR) resolution modes. In the HR mode only data from directly opposing detectors are employed. In the MR and LR the coincidence data of 2 and 4 neighboring detectors which view a common point at the center of the detector field of view are added to the data in the HR mode. The resolution in the HR, MR and LR are all the same at the center line of the field of view but above and below this line the MR and LR vary with distance due to angulation of the additional lines of response. The HR mode has constant resolution in depth. The different resolution modes allow selection of the best compromise between resolution and efficiency for particular imaging situations. Since the data for all modes are collected and stored during each scan the user can select any or all resolution modes for display.

The scan time in the rectilinear mode can be selected for a fixed time or fixed number of counts with typical whole body scan times from 10 to 50 min. Scans can also be performed in a transmission or emission mode. An external ring source of positron activity which fits in a track of the center hole of the tomograph is counted without and with the subject in place; the ratio of these two measurements is the photon attenuation in the subject.

The transmission data is used to either correct the emission image for attenuation, for morphological identification or used independently for setup of the patient for the emission scan (ie, see Fig. 14).

The rectilinear 2-D scanning mode is used for the following:

i) whole body or limited field organ scanning to determine the distribution, uptake and retention of the administered compound. Correction for photon attenuation allows the quantification of the above parameters.

ii) set up and selection of levels to be studied in detail by ECT. This significantly improves the efficiency of ECT and removes much of the guess work of setup. Once the 2-D image appears on the display screen the user selects the levels of interest with the joy stick, the computer moves the patient to this level and the ECT sequence is initiated.

iii) to provide an overall perspective of the region studied by ECT.

TRANSAXIAL TOMOGRAPHIC MODE

The tomographic scans are performed by a combination of linear scans of the detector banks over a distance of 4 cm followed by a rotation of the gantry through a discrete angle. This sequence is carried out through an angle of 60° for complete scan (Fig. 2). The computer then indexes the patient bed to the next position (ie, next slice) and the scanning sequence is repeated in the opposite direction. The data are corrected for radioactive decay, sorted, normalized, corrected for photon attenuation, reconstructed with a convolution based algorithm and displayed. Variable linear and angular sampling is inherent in the ECAT design and any linear and angular sampling resolution which is multiple or submultiple of 0.57 cm

and 2.5°, respectively can be employed. This assures that there need not be any sampling limitations which could restrict image resolution and contrast or produce sampling artifacts. Some typical sampling options are shown in Table I. It should be noted that due to the geometric design of the ECAT that even though data are collected at 5°, 7.5° or 10° increments they are sorted into linear scan profiles that are separated by only 2.5°.

Scan times are selectable from 10 sec/slice to multiple mins/slice. Scan times/slice can be selected for a fixed time, fixed total number of counts or can be automatically increased from one slice to the next to compensate for radioactive decay of the administered radionuclide. The number of slices to be studied may be selected by the user and are subsequently scanned automatically (ie, via computer control of bed).

The image resolution is determined by the sampling resolution, inherent detector resolution (ie., with or without shadow shields in place) and reconstruction filter function employed. Typical resolution values are shown in the phantom section but a number of different combinations of the above factors are employed to optimize image resolution, contrast and signal/noise for different types of studies performed. The present reconstruction time is about 55 seconds for the typical 100 x 100 display format. However, total time from end of scan to image display is about 2 min. due to additional time for attenuation correction and display. (Work is in progress to shorten this time).

Attenuation correction is applied from either a transmission measured correction or geometric correction as discussed elsewhere (9,31). Phelps et al. (31) have shown from measurements in human subjects, that the average path length attenuation with ACD in the head, abdomen and thorax vary about

±3%, ±8% ±28% (±1 std deviation), respectively and therefore the measured attenuation correction is only used for heart studies.

The ECAT can also be calibrated with a uniform phantom containing a known activity concentration such that the images from a subject can be displayed and read directly in concentration units of μCi/cc or metabolic rates in mg/min/100 gms (ie, with incorporation of a physiologic model of metabolism).

The subject is positioned in the ECAT with the aid of a low power neon laser and a selected series of ECT scans can be carried out automatically. Alternatively, transmission or emission rectilinear scans can be used interactively through the joy stick to select appropriate levels to be scanned by ECT.

PHANTOM STUDIES

RESOLUTION

ECT: As discussed above a number of different resolution capabilities exist for the ECAT. However, typical values for the high, medium and low resolution mode in the transaxial tomographic format are shown in Figure 4. These values were obtained with 2 mm diameter line sources (^{64}Cu) in a 20 cm diameter solid plastic phantom as a scattering media. The resolution across the transaxial plane has a measured uniformity of < 1 mm. The measured resolution in the axial direction is 1.8 cm without the shadow shields and 1.9 cm with the shadow shields.

Rectilinear: The resolution was measured with 2 mm diameter line sources in a 20 cm thick scattering media. In the high resolution mode (ie., using only straight across line of coincidence) the FWH resolutions are 0.85 ± 0.1, 1.3 ±0.1 and 1.7 ± 1 cm with the 1.5 cm, 2.3 cm shadow shields and no shadow shields, respectively. In this mode resolution is constant with depth. Due

to the use of some angulated lines of response the medium and low resolution mode resolutions vary in depth. The medium resolution mode increases the FWHM by an average of 0, 3 and 6 mm at the center of the field of view (FOV) and 7.5 and 14 cm from the center of the FOV. For example, with a 15 and 28 cm diameter object the resolution across the center of the object is the same as the high resolution mode but progressively worsens by 3 mm at the outer edge of the 15 cm diameter object or progressively worsens by 6 mm at the outer edge of the 28 cm diameter object. The resolution in the low resolution mode worsens by 0, 6 and 15 mm at the center line, 7.5 and 14 cm from center line. Across the retilinear image, resolution at any given depth varies $\leq$ 1 mm.

EFFICIENCY

ECT: The efficiency was measured with 15 and 20 cm diameter cylinders filled with positron activity (^{18}F). The values without and with the 2.3 cm and 1.5 cm diameter shadow shields are listed in Table 2. As a measure of efficiency the count rate/activity concentration was determined for a uniform distribution of activity in a cylindrical phantom. This was considered more realistic than line or point sources in air since it reflects the actual imaging situation (ie., distributed activity in an attenuating media). However, in stating efficiency with a distributed source, one must acknowledge the fraction of counts due to scatter coincidence (see section on in plane scatter) and random coincidence. The efficiency values listed in Table 1 contain < 1% random coincidences.

These relatively small diameter phantoms were chosen to allow comparison to systems with smaller FOV than the 50 cm field of the ECAT (ie., systems designed to have maximum efficiency for a small FOV). The large FOV of the

ECAT is employed to allow any portion of the human body to be examined without distortions due to field size limitations.

The efficiencies in Table 1 can be compared at the same resolution to the PETT III with the 3.8cm shadow shields of 10,000 c/sec/μCi/cc[4] (this corresponds to low resolution mode of ECAT in Table 2) with a 20 cm diameter phantom[5] and the ring system being developed by Derenzo and Budinger of 11,300 c/sec/μCi/cc[4] in a 20 cm phantom with a resolution that is about 8 mm (circular) at the center of the 30 cm FOV, 8 x 13 mm and 8 x 19 mm (eliptical) at 10 and 15 cm from center, respectively (32). In this comparison it should be noted that the resolution of the Derenzo-Budinger ring is about 50% better than ECAT in the axial direction.

The detection efficiency of the ECAT decreases as the exposed detector diameter is decreased with the shadow shields (Table 1). However, this decrease is not as rapid as would be expected from geometric considerations (25) because the shielded or covered part of the detector acts as a "catcher" for the 511 KeV photons which enter through the holes in the shadow shields. This is an important consideration in choice of detector sizes (ie, efficiency vs resolution) due to the difficulty of detecting 511 KeV photons.

Rectilinear: The rectilinear scan efficiency is 0.09, 0.27 and 0.45 times the efficiency for ECT for the high, medium and low resolution rectilinear scan modes for a 20 cm diameter phantom. Again remembering that this phantom size is not employing the total efficiency of the 50 cm FOV of the ECAT.

LINEARITY AND COUNT RATE CAPABILITY

The system linearity and count rate capability were evaluated by filling a uniform 20 cm diameter phantom with a water solution of ^{13}N-ammonia and recording the system count rate as a function of time. The 10.0 min half life

---

[4]Efficiency value assumes 100% positron emission/μCi.

[5]Unpublished data (Hoffman, Phelps).

decay of ^{13}N was used to examine the deviation from a true count rate. Figure 5 illustrates that the ECAT linearity is excellent in the count rate range of $\leq$ 20,000 c/sec in which it is typically employed.

RANDOM COINCIDENCE

The same phantom used above was also employed in the measurement of the random coincidence fraction at several different system count rates. These values are shown in Table 3. The random coincidence fraction increases with system count rate since the random coincidence count rate is proportional to the (amount of radioactivity)^2 whereas the true coincidence count rate is directly proportional to amount of radioactivity.

SCATTER COINCIDENCE

We determined the magnitude of true coincidence resulting from scattered radiation produced by activity in and out of the plane of the FOV. The fraction occurring from outside the FOV was measured with a phantom that was 16 cm long and 20 cm in diameter which had a 4 cm long section in the center that could be filled separately with activity or water. The phantom was initially filled with activity including the center section and positioned (ie, the 16 cm length in the axial direction of the ECAT) with the 4 cm section in the FOV of the ECAT. The total coincidence count rate was recorded and then the activity in the 4 cm section was replaced with water and the count rate measured again. The second count rate represents the coincidence events due to scattered radiation from the activity above and below the FOV (out of plane scatter). This fraction was found to be 5.4% of the true coincidence count rate.

The scatter from activity within the FOV (in plane scatter) was measured with a 20 cm diameter x 4 cm thick plastic phantom which contained a single line source. Separate measurements were performed with the line source at

the center of the phantom, 5 cm from center and 9 cm from center of the phantom. The fraction of scatter was then determined for selected linear scan profiles from the 72 angular projections by measuring the number of counts outside of the 3.8 cm (ie, detector diam.) wide portion of the line spread function and dividing this value by the total number of counts recorded in the full FOV and the 20 cm diameter of the object. These values were found to be 10.3% and 6.1%, respectively. Thus, the total scatter fractions (ie, in plus out of plant) is about 15.4 and 7.1% for the full 50 cm FOV and a 20 cm diameter object, respectively. These scatter fractions are worse case values since they were measured in LR mode (ie, MR and HR modes will have lower scatter fractions because they have lower solid angle efficiencies). These scatter fractions are similar, although somewhat lower, than those reported by Derenzo (24) of 18% for the 30 cm FOV Donner ring system. The somewhat lower value for the ECAT is understandable since it has larger detectors with a higher 511 KeV/low energy (ie, scatter radiation) detection efficiency and a larger separation distance between detectors (100 cm compared to 80 cm for Donner camera which provides a better solid angle discrimination against scatter:scatter fraction is inversely proportional to detector solid angle efficiency). The Donner ring system has somewhat better slit shielding than the ECAT and therefore the differences are less than would be predicted from considerations given above. These scatter fractions are also considerably lower than the values of 40 to 60%, depending on the amount of pulse height analysis, for the Searle Radiographics[6] positron camera without slit shields (33).

It should also be noted that in the ECT mode the scatter and random coincidence fractions are substantially reduced in the final image as a result of an inherent deemphasis (low weighting) in the reconstruction process due to their low frequency nature. For example, if the scatter plus random coincidence fraction were 15% in the collected data, this fraction is reduced to about 6% in the reconstructed image of a 20 cm diameter object.

[6]Searle Radiographic, Chicago, Illinois.

ACCURACY AND FIELD UNIFORMITY

ECT: The accuracy of the reconstructed image is a function of many factors: statistics, accuracy of attenuation correction, amount of scattered radiation and random coincidences, detector stability, data losses due to dead time, mechanical positioning accuracy, motion artifacts, sampling errors, spatial response of detector relative to assumption of reconstruction algorithm, relationship of the shape of the reconstruction filter to inherent detector resolution, linear and angular sampling and statistics, etc. Many of these factors are difficult if not impossible to define in a general way since they are all interrelated and their magnitude is in great part a function of the particular tomographic design. Many of these factors have been discussed elsewhere (8-10, 25-31, 34-36). Phantom studies were carried out to examine the total effect of these factors without particular attention to them individually.

A 20 cm diameter phantom containing a uniformily distributed source of positron activity (^{68}Ga) was imaged for different total times to collect 20,000,000, 1,000,000 and 500,000 total counts. The % standard deviation (% SD) from the mean picture element value was then calculated over the center 15 cm section of the image (ie, to avoid edge effects). The average theoretical % S.D. was also calculated assuming the only source of error was statistical in origin as given by:

$$\% \text{ S.D.} = 0.75 \left[D^3/(2 (\Delta X)^3 N)\right]^{\frac{1}{2}} \times 100 \qquad (1)$$

where D, ΔX and N are the object diameter, linear sampling distance and total number of counts in the image, respectively. Eq. 1 assumes a Shepp (37) reconstruction filter function, with a cut off frequence of $(2\Delta X)^{-1}$ and linear interpolation in the back projection. Eq. 1 is similar to the equations

derived by Chesler et al. (35) and Budinger et al. (34). The measured S.D. errors at 20 million, 1 million and 0.5 million total counts were found to be less than or equal to the theoretical statistical predictions down to a value of about 1.4% (Fig. 6). This indicates that the noise component in the ECT images of the ECAT is primarily due to photon statistics. A significant factor in the accuracy of the ECAT results from the redundant sampling in which each data point is repeatedly sampled by different detectors throughout the scan (31). The redundant sampling employed in the ECAT also increases efficiency from the edge to the center of the object to offset partially the effects of photon attenuation and error propogation in CT which increase error from edge to center (31,33).

A phantom which simulated the brain was imaged under different conditions: i) stationary position with all detectors in calibration, stationary position with the center 11 and 33 coincidence lines of response (ie, center positions where maximum reinforcement of error occurs) disconnected; and ii) the phantom was moved 20 times descretely in one direction (ie, toward and away from one detector bank pair; a worse case motion) over a total distance of 1.5 cm during the scan. The minor distortions that occurred during these studies (Figs. 7 & 8) result from the inherent protection provided by the redundant data sampling feature of the ECAT. If a study is performed with the detectors out of calibration any resulting artifacts can be removed by reconstructing the image after recalibration (Fig. 8).

HUMAN AND ANIMAL STUDIES

RECTILINEAR SCAN STUDIES

Figure 9 shows a whole body rectilinear scan of a normal human subject

5 minutes after the inhalation of 10 mCi of ^{11}CO. Since ^{11}CO binds to hemoglobin this shows the blood distribution. A whole body transmission scan is also shown.

Figure 10 shows the whole body distribution of ^{18}F-2-deoxyglucose (^{18}FDG) in a 20 Kg dog along with the transmission image and the emission image after correction for photon attenuation using the transmission data. This illustrates the use of combined transmission-emission data to provide quantitative information for measurement of radiopharmaceutical distributions.

A whole body rectilinear bone scan of a normal 20 Kg dog 60 minutes after the I.V. administration of 3.5 mCi of $^{18}F^-$ in physiologic saline is shown in Figure 11.

Figure 12 shows the whole body rectilinear and ECT scans of a 26 year old patient with Hodgkins lymphoma. The rectilinear scan was carried out 2 hours post I.V. injection of 5 mCi of $^{18}F^-$ in physiologic saline. Multiple metastasis are seen in the calvarial region, lower thoracic and lumbar spine region, right greater trochanter, distal two-thirds of the left femor and left iliac crest. All of the confirmed lesions seen on the ^{18}F ECAT scan were also seen in a ^{99m}Tc-HEDSPA scan. The calvarial lesions were somewhat better seen on the ^{99m}Tc-HEDSPA scan whereas the remainder were equally well seen on both exams with the exception that an apparent lesion in the right shoulder was better seen in the ^{18}F scan and a focus of ^{18}F uptake was also noted in the mid cervical spine in the ECAT scan.

Prior to the rectilinear scans (1 hour post injection) 12 ECT scans were taken from 4 cm above the iliac crest in 18 mm steps down to the greater trochanter (Fig. 12). High uptake of ^{18}F is noted in left iliac crest at the 7th level and in the head of the right femur of the 12th level.

EMISSION COMPUTED TOMOGRAPHY

Where the rectilinear images shown above clearly display a wide range of information they are limited in detailed evaluations. This is illustrated in comparing the ^{11}CO rectilinear scan in Figure 9 with the ^{11}CO ECT scans of the brain shown in Figure 13. The ECT scans show the detailed distribution of cerebral blood volume (CBV). The data from Figure 13 can be used to calculate the CBV in units of cc of blood/gm of tissue (39-41).

Figure 14 illustrates both the use of transmission and emission limited field rectilinear scans for the interactive selection of levels to be examined in detail with ECT. The rectilinear scans at the bottom of Figure 13 were taken (3 mins/scan), displayed on the viewing screen and the joy stick used to select the starting level (indicated by x) for ECT. The computer then automatically moved the patient to the position indicated and performed a selected sequence of ECT scans. Even though this study was ungated, note the delineation of the vascular structures of and surrounding the heart.

Figure 15 shows a series of ECT images of the thorax in a human subsequent to the I.V. injection of ^{18}FDG. These images illustrate the use of ECT and ^{18}FDG to image the cross sectional distribution of glucose metabolism in the myocardium (42,43).

Representative ECT images of the brain following an I.V. of $^{13}NH_3$ and ^{18}FDG in human subject are shown in Figure 16. The $^{13}NH_3$ images are considered to reflect the distribution of capillary density (and possibly perfusion) in the brain (41, 44) whereas ^{18}FDG images represent the distribution of the cerebral metabolic rate for glucose, CMRGlu (45-47). Quantitative studies have been carried out on normal volunteers with ^{18}FDG in which the ECT values for CMRGlu in regional areas of cortex, internal grey nuclei and subcortical white matter

are in excellent agreement with values in the literature from autoradiographic studies in monkeys and with hemispheric values in man (46). Note the delineation of the superficial cortex, visual cortex, internal grey nuclei in the region of the basal ganglia (ie, caudate nucleus, thalamus etc.) and subcortical white matter in both the $^{13}NH_3$ and ^{18}FDG images in Figure 16. Direct correspondence in the $^{13}NH_3$ and ^{18}FDG images have been observed in normal regions of the brain in our studies with human subjects (47). If $^{13}NH_3$ represents cerebral perfusion, then this would be expected since perfusion is normally regulated by regional metabolic activity.

Figure 17 shows selected ECT levels from an $^{13}NH_3$ and $^{68}GaEDTA$ studies with the ECAT and a x-ray CT study of a 23 year old patient with a right occipital infarct. The $^{13}NH_3$ and $^{68}GaEDTA$ clearly demonstrate a perfusion and blood brain barrier defect (arrow). The x-ray CT scan was negative. The brain slices (not the same patient) are shown for anatomical comparison of the highly perfused superficial cortex, visual cortex and grey nuclei in basal gnaglia (caudate nucleus, thalamus, mesencephalon) seen in $^{13}NH_3$ images.

A 70 year old patient with a glioblastoma in the right frontal lobe was studied with $^{68}GaEDTA$, $^{13}NH_3$ and x-ray CT (with contrast enhancement) as shown in Figure 19. The tumor was clearly seen in ^{68}Ga EDTA and x-ray CT studies. The $^{13}NH_3$ scan at O.M. + 7 cm showed apparent reduced perfusion throughout the entire right hemisphere coinciding with edema seen in the EMI scan, apparent reduced perfusion (OM + 5.2, + 3.4 and + 1.6) at the site of the tumor and apparent increased perfusion (arrows to dark areas) at the periphery of the tumor. Note regions of low apparent perfusion (arrows to light areas) coinciding with edema seen on x-ray CT scan. The lack of perfusion in the edemous tissue could occur because of increased tissue pressure with a loss of autoregulation (ie, passive constriction or collapsing of vessels). A possible ischemic area is seen at OM + 1.6 but this was not observed by any

other examination.

CONCLUSION

The ECAT is a complete positron imaging system capable of providing high contrast, high resolution, quantitative images in both a 2 dimensional and tomographic format. The flexibility of this system in its various image mode options allows it to be used for a wide variety of imaging problems.

The geometric and physical design of the ECAT inherently provides for high image quality. Geometric discrimination against coincidence from scattered radiation is accomplished by using relatively large detector bank separation distanced (100 cm) and well designed single plane slit shields which reduce detection of radiation originating outside the plane of interest. The detection ratio of scattered to unscattered coincidence is inversely proportional to the square of the distance between detectors (ie, doubling d reduces scatter fraction by 4). Increasing d also reduces the true coincidence efficiency per detector pair by d^2. However, as d increases more detectors can be added and since the detection efficiency in annihilation coincidence detection increases as the square of the number of detectors (8) this completely offsets the reduction in efficiency for each detector. Therefore, the large detector separation distance reduces the scatter fraction without any loss of system detection efficiency. Since the scatter fraction is also directly proportional to the 3rd power of the opening in the slit shields (23) this design aspect of the ECAT further reduces the scatter fraction.

The relatively large value of d also provides better uniformity of resolution with depth (8-11).

Since the random coincidence fraction is also inversely proportional to d^2, the ECAT design exhibits a low occurrence of random coincidences. The slit shields and detector shielding dramatically reduces random coincidences by

reducing the detector count rates from photons originating outside the plane of interest (ie, random coincidence rate is proportional to the 4th power of slit shield opening (23)).

The detector size (3.8 cm x 7.6 cm) used in the ECAT provides high detection efficiency and further improves the ratio of true to random coincidence while still allowing high resolution. Shadow shielding of detectors provides flexability in selectable trade offs between resolution and efficiency which is backed with high sampling resolution.

All of the above factors improve contrast, quantitative accuracy and count rate capability.

The redundant sampling feature of the ECAT provides improved accuracy and uniform error distribution compared to uniform sampling system designs (ie, SPC systems and circular ring ACD systems). Redundant sampling also provides protection against detector instabilities and artifacts due to activity, organ or patient movement.

The fast scanning capabilities, high detection efficiency, automatic programmed scanning sequences, and interactive 2D and 3D imaging capabilities increase the overall imaging efficiency and improve the accuracy of the study. High detection efficiency of ECAT allows short scan times and/or high statistical image quality (ie, > million c/min. for $^{13}NH_3$ and ^{18}FDG in brain and ^{11}CO in heart per 20 mCi at LR; MR & HR values can be determined from Table 2).

Quantitative image accuracy appears to be primarily limited by photon statistics rather than algorithm, mechanical or electronic errors down to a level of ± 1.4%. Accurate and convenient attenuation correction of ACD is also a major factor in overall image accuracy. The magnitude of error introduced into actual patient studies from the geometric attenuation (ie, from discrepancies between shape of cross section and the assumed eliptical shape and use of a single value of attenuation coefficient) or statistical error when the transmission

measurement is employed needs to be studied in more detail.

A variety of different types of studies are presented to illustrate the imaging capabilities of the ECAT in a number of different procedures. However, these studies also serve as examples of the non-invasive study methods which have been made possible through the development of ECT. It should be appreciated that ECT not only provides improved image quality through tomography but more importantly it allows one to perform a measurement that has not been possible or methodologically limited by other approaches. ECT allows one to quantitatively measure a physiologic process with a new dimension in detail and accuracy while still maintaining the non-invasive aspect of the method. The quantitative format and physiologic models for ECT are exemplified by analogy to autoradiography. However, ECT allows studies to be carried in the living viable animal or patient setting (26,27).

Where x-ray CT and ultrasound are providing a highly effective method for the detection of a variety of human diseases, the complete assessment of patient statis for proper management is still limited. The evaluation of metabolism, blood flow and volume, vessel permeability, anaerobic-aerobic ratios, metabolic shunts, tissue acidosis and a variety of other functions, on a regional organ basis would improve our understanding of human disorders. Probably the greatest potential of this technique is in the detection, investigation and characterization of disease at a stage when it is reversible and to provide information for more decisive treatment or treatment evaluation. The study of diseases which are not associated with focal lesions, but occur from hereditary or developing loss of function (ie, degenerative metabolic or vascular diseases) could also be improved through the use of ECT.

Quantitative instrumentation is only one factor in the measurement of physiologic processes. Labeled substrates or physiologic analogs whose kinetics are understood and describable with physiologic models are required. This appears as one of the rate limiting steps for the growth of this technique. On one hand

there are the positron emitting isotopes of ^{11}C, ^{13}N and ^{15}O which are natural elements for labeling compounds without disturbing their biological or chemical behavior. These labeled compounds are supported by the optimal imaging properties of coincidence detection in a quantitative imaging format. However, due to the short half lives of these isotopes a on-site accelerator is required. The development of positron tomography has stimulated work in the area of better defining the requirements and accelerator design possibilities for an effective accelerator based generator system specifically designed to meet the requirements of a medical environment and the needs of ECT.

^{18}F is a commercially available positron radioisotope which can be used for labelling physiologic analogs as exemplified by the development of ^{18}F-2-deoxyglucose by Wolf's group at Brookhaven (38). ^{68}Ga from a commercial generator (^{68}Ga) can also be used to label potentially useful compounds for positron tomography but may be limited to the more conventional form of radiopharmaceuticals.

On the other hand single photon counting (SPC) approaches have the advantage of readily available isotopes (principally ^{99m}Tc but also ^{201}Tl, ^{131}I and ^{123}I). Where these isotopes can be used to label physiologically active compounds the in vivo stability and physiologic integrity of the labeled compound have generally been difficult to maintain. Labelled compounds which are carefully "designed" to minimize the perturbation of the compounds bio-specific properties and to provide in vivo stability would allow new advances with SPC tomography. Where SPC tomography has been successful in studies of the brain, limited success has been achieved to date for whole body studies (29).

It would appear that much of the success of ECT and the technique of choice will be determined in large degree by the type of compounds and physiologic models that can be developed.

The unique potential of this developing modality exist in the measurement

and use of physiologic parameters and investigative efforts should resist the use of radiopharmaceuticals as contrast enhancement materials for the detection of disease as so often has occurred in the past. If this goal can be achieved *physiologic tomography* will provide important information not obtainable from the primarily morphologically oriented techniques of x-ray CT and ultrasound.

REFERENCES

1. Kuhl, D.E., Edwards, R.Q., Ricci, A.R., et al: The MARK IV System for Radionuclide Computed Tomography of the Brain. Radiology 121: 405-413, 1976.
2. Kuhl, D.E., Hoffman, E.J., Phelps, M.E., et al: Design and Application of the MARK IV Scanning System for Radionuclide Computed Tomography of the Brain. (IN): IAEA SM-210/99 Medical Radionuclide Imaging, Vol 1, pp 309-320, 1977.
3. Bowley, A.R., Taylor, C.G., Causer, D.A., et al: A Radioisotope Scanner for Rectilinear, Arc, Transverse Section and Longitudinal Section Scanning: (ASS-The Aberdeen Section Scanner). Br J. Radiol 46:262-271, 1973.
4. Keyes, J.W., Orelandea, N., Heetderks, W.J., et al: The Humongotron-A Scintillation Camera Transaxial Tomograph. J. Nucl Med 18:381-387, 1977.
5. Budinger, T., Gullberg, G.T.: Three-dimensional Reconstruction in Nuclear Medicine by Iterative Least-Squares and Fourier Transform Techniques. IEEE Med Sci NS-21:2-20, 1974.
6. Budinger, T.F., Gullberg, F.T.: Transverse Section Reconstruction of Gamma-ray Emitting Radionuclides in Patients. (IN) Reconstruction Tomography in Diagnostic Radiology and Nuclear Medicine. Ter-Pogossian, M.M, Phelps, M.E., Brownell, G.L., et al (Eds) 1977, University Park Press, 315-342.
7. Jaszcaak, R.J., Murphy, P.H., Huard, D., et al: Radionuclide Emission Computed Tomography of the Head with ^{99m}Tc and a Scintillation Camera. J. Nucl Med 18:373-380, 1977.
8. Phelps, M.E., Hoffman, E.J., Mullani, N.A., et al: Application of Annihilation Coincidence Detection to Transaxial Reconstruction Tomography. J. Nucl Med 16:210-233, 1975.

9. Phelps, M.E., Hoffman, E.J., Mullani, N., et al: Design and Performance Characteristics of a Whole Body Transaxial Tomograph (PETT III). IEEE Nucl Sci NS-23:516-522, 1976.

10. Hoffman, E.J., Phelps, M.E., Mullani, N., et al: Design and Performance Characteristics of a Whole Body Transaxial Tomograph. J. Nucl Med 17: 493-503, 1976.

11. Ter-Pogossian, M.M., Phelps, M.E., Hoffman, E.J., et al: A Positron Emission Transaxial Tomograph for Nuclear Medicine Imaging (PETT). Radiology 114:39-93, 1975.

12. Ter-Pogossian, M.M.: Basic Principles of Computed Axial Tomograph. Sem Nucl Med 7:109-128, 1977.

13. Brownell, G.L., Burnham, C.A.: (IN) Tomographic Imaging in Nuclear Medicine, Friedman, G.S., (Ed) New York, Soc Nucl Med (1973) pp 154-164.

14. Brownell, G.L., Burnham, C.A., Chesler, D.A., et al: Transverse Section Imaging of Radionuclide Distributions in Heart, Lung, and Brain. (IN) Reconstruction Tomography In Diagnostic Radiology and Nuclear Medicine. Ter-Pogossian, M.M., Phelps, M.E., Brownell, G.S., et al (Eds). Baltimore, University Park Press (1977) pp 293-307.

15. Muehllenhner, G., Buchin, N.P., Dubek, G.H.: Performance Parameters of the Positron Imaging Camera. IEEE, Nucl Sci, NS-23:528-537, 1976.

16. Muehllenhner, G., Atkins, F., Harper, P.V.: Positron Camera with Longitudinal and Transverse Tomographic Ability. IAEA-SN-210/84, 1975 (In Press).

17. Lim, C.B., Chu, D., Kaufman, L., et al: Initial Characterization of a Multi-Wire Proportional Chamber Positron Camera. IEEE Nucl Sci, NS-22, 388-394, 1975.

18. Hattner, R.S., Lim, C.B., Swann, S.J., et al: Cerebral Imaging Using ^{68}Ga-DTPA and the UCSF Multi-Wire Proportional Chamber Positron Camera. IEEE Nucl Sci NS-23, 523-525, 1976.

19. Robertson, J.S., Marr, R.B., Rosenblum, B., et al: 32 Crystal Positron Transverse Section Detector. (IN) Tomographic Imaging in Nuclear Medicine, Freedman, G.S. (Ed) New York, Society of Nuclear Medicine, 1973, pp. 142-153.

20. Yamamoto, Y., Thompson, C.J., Meyer, E., et al: Dynamic Positron Emission Tomography for Study of Cerebral Hemodynamics in a Cross-Section of the Head Using Positron-Emitting ^{68}Ga-EDTA and 77 Kr. J. Comput Assisted Tom 1:43-56, 1977.

21. Cho, Z.H., Eriksson, L., Chan, J.: A Circular Ring Transverse Axial Positron Camera. (IN) Reconstruction Tomography and Diagnostic Radiology in Nuclear Medicine. Ter-Pogossian, M.M., Phelps, M.E., Brownell, G.L., et al (Eds), Baltimore, University Park Press (1977) pp 393-424.

22. Cho, Z.H., Cohen, M.B., Singh, M., et al: Performance and Evaluation of the Circular Ring Transverse Axial Positron Camera (CRTAPC). IEEE Nucl Sci, NS-24, 530-543, 1977.

23. Derenzo, S.E., Zaklad, H., Budinger, T.F.: Analytical Study of a High-resolution Positron Ring Detector System for Transaxial Reconstruction Tomography. J. Nucl Med 16:1116-1173, 1975.

24. Derenzo, S.E., Budinger, T.F., Cahoon, J.L., et al: High Resolution Computed Tomograph of Positron Emitters. IEEE, Nucl Sci, NS-24, 544-558, 1977.

25. Hoffman, E.J., Phelps, M.E.: An Analysis of Some of the Physical Aspects of Positron Transaxial Tomography. Comput. Biol Med 6:345-360, 1976.

26. Phelps, M.E.: What is the Purpose of Emission Computer Tomography in Nuclear Medicine. J. Nucl Med 18:399-402, 1977.

27. Phelps, M.E., Hoffman, E.J., Kuhl, D.E.: Physiologic Tomography: A new Approach to In Vivo Measure of Metabolism and Physiological Function. (IN) Medical Radionuclide Imaging, Vol. 1, IAEA, Vienna, pp 233-253, 1977.

28. Phelps, M.E., Hoffman, E.J., Huang, S.C., et al: Positron Tomography: "In Vivo" Autoradiographic Approach to Measurement of Cerebral Hemodynamics and Metabolism. (IN) Cerebral Function, Metabolism and Circulation. Ingvar, D.H., Lassen, N.A. (Eds) Munksgaard, Copenhagen (1977) pp 446-447.

29. Phelps, M.E.: Emission Computed Tomography. Sem Nucl Med (Oct, 1977).

30. Phelps, M.E., Hoffman, E.J., Gado, M., et al: Computerized Transaxial Transmission Reconstruction Tomography (IN) Non-Invasive Brain Imaging, Computed Tomography and Radionuclides. DeBlanc, H., Sorenson, J. (Eds), New York, Soc Nucl Med, 1975, pp 111-146.

31. Phelps, M.E., Hoffman, E.J., Mullani, N.A., et al: Some Performance and Design Characteristics of PETT III. (IN) Reconstruction Tomography in Diagnostic Radiology and Nuclear Medicine. Ter-Pogossian, M.M., Phelps, M.E., Brownell, G.L. et al (Eds) Baltimore, University Park Press (1977) pp 371-392.

32. Derenzo, S.E.: Positron Ring Cameras for Emission-computed Tomography. IEEE, NS-24, 881-885, 1977.

33. Muehllenhner G.: Private Communication.

34. Budinger, T.F., Derenzo, S.E., Gullberg, G.T., et al: Emission Computed Axial Romography. J. Compt Assist Tomo 1:31-45, 1977.

35. Chesler, D.A., Aronow, S., Correll, J.E., et al: Statistical Properties and Stimulation Studies of Transverse Section Algorithms. (IN) Reconstruction Tomography in Diagnostic Radiology and Nuclear Medicine. Ter-Pogossian, M.M., Phelps, M.E., Brownell, G.L. et al (Eds) Baltimore, University Park Press (1977) pp 49-58.

36. Zacher, R.: Resolution Limit for Reconstruction Tomography Based on Photon Attenuation. (IN) Reconstruction Tomography in Diagnostic Radiology and Nuclear Medicine. Ter-Pogossian, M.M., Phelps, M.E., Brownell, G.L. et al (Eds) Baltimore, University Park Press (1977) pp 59-66.

37. Shepp, L.A., Logan, B.F.: Some Insights into the Fourier Reconstruction of a Head Section. IEEE Nucl Sci, NS-21, 21-43, 1974.

38. Ido, T., Wan, C.N., Casell, V. et al: Labeled 2-Deoxy-D-glucose Analogs. ^{18}F-Labeled 2-Deoxy-2-Fluoro-D-glucose, 2-Deoxy-2-Fluoro-D-Mannose and ^{14}C-2-Deoxy-2-Fluoro-D-Glucose. J. Labelled Comp & Radiopharm (In Press).

39. Phelps, M.E., Grubb, R.L., Jr., Ter-Pogossian, M.M.: In Vivo Cerebral Blood Volume by X-ray Fluorescence: Validation of Method. J Appl Physiol 35:741-747, 1973.

40. Kuhl, D.E., Reivich, M., Alavi, A., et al: Local Cerebral Blood Volume Determined by Three-Dimensional Reconstruction of Radionuclide Scan Data. Circulat Res 36:610-619, 1975.

41. Phelps, M.E., Hoffman, E.J., Coleman, R.E., et al: Tomographic Images of Blood Pool and Perfusion in Brain and Heart. J Nucl Med 17:603-612, 1976.

42. Phelps, M.E., Hoffman, E.J., Highfill, R. et al: A New Emission Computed Axial Tomograph for Positron Emitters. J Nucl Med 18:603, 1977.

43. Gallagher, B.M., Ansaii, A., Atkins, H. et al: Radiopharmaceuticals XXVII. ^{18}F-labelled 2-deoxy-2-fluoro-D-glucose as a radiopharmaceutical for measuring regional myocardial glucose metabolism in vivo: Tissue distribution and imaging studies in animals. J Nucl Med 18:990-996, 1977.

44. Phelps, M.E., Raichle, M.E., Hoffman, E.J., et al: Factors which affect uptake and retention of $^{13}NH_3$. Stroke (In Press) Nov, 1977.

45. Sokoloff, L., Reivich, M., Kennedy, C., et al: The (^{14}C) Deoxyglucose Method of the Measurement of Local Cerebral Glucose Utilization: Theory, Procedure and Normal Values in the Conscious and Anesthetized Albino Rat. J Neurochem 28:897-916, 1977.

46. Reivich, M., Kuhl, D.E., Wolf, A., et al: Measurement of local cerebral glucose metabolism in man with ^{18}F-2-Fluro-2-deoxy-D-glucose.(IN) Cerebral Function, Metabolism and Circulation. Ingvar, D.H., Lassen, N.A. (Eds) Munksgaard, Copenhagen, 1977, pp. 190-191.

47. Kuhl, D.E., Phelps, M.E., Hoffman, E.J., et al: Initial Clinical Experience with ^{18}F-2-Deoxy-D-glucose for Determination of Local Cerebral Glucose Utilization by Emission Computed Tomography. (IN) Cerebral Function, Metabolism and Circulation. Ingvar, D.H., Lassen, N.A. (Eds) Munksgaard, Copenhagen, 1977, pp. 192-193.

ACKNOWLEDGEMENTS

We wish to thank Dr. Norman S. MacDonald and his cyclotron staff and Dr. Gerald Robinson and his chemistry staff for the production of the compounds used in this study and Miss JoAnn Miller, Miss Francine Aguilar and Mr. Carl Selin for technical help. Thanks are due to Miss Lee Griswold and Mr. Hector Pimentel for illustration work. Acknowledgement is given to Dr. Wolf's group at Brookhaven National Laboratory who developed and built the targetry used for the production of ^{18}FDG.

TABLE 1.

SOME TYPICAL ECT SCAN OPTION WITH ECAT

Mode	Angular Scan* Increments	Linear Scan Increments	Image Resolution	Scan Time
High Resolution	5°	8 (5.7 mm/increment)	0.95, 1.3 cm	⩾ 1 min/slice
High Resolution Head	10°	"	"	⩾30 sec/slice
Medium Resolution	5°	"	1.3 or 1.6 cm	⩾ 1 min/slice
Medium Resolution Head	10°	"	"	⩾30 sec/slice
Low Resolution	5°	4 (1.14 cm/increment)	2.2 cm	⩾ 1 min/slice
Low Resolution Head	10°	"	"	⩾30 sec/slice
Rapid Scan	7.5°	"	"	⩾10 sec/slice

*Even though angular scanning increments are 5, 7.5 and 10° the data are sorted into linear scan profiles at angular increments of 2.5° for reconstruction.

TABLE 2.

SYSTEM EFFICIENCY† VERSUS RESOLUTION

Average Detector Pair Resolution (FWHM)*	Image Resolution (FWHM)	Image Mode	15 cm diam. phantom (counts/sec/μCi/cc)	20 cm diam. phantom (counts/sec/μCi/cc)
1.6 cm	1.7 cm	Low Resolution	25,100	30,100
1.1 cm	1.3 cm	Medium Resolution	13,500	15,900
0.8 cm	0.95 cm	High Resolution	7,730	9,200

†Efficiency is given for 100% positron emission/μCi. Fraction of random coincidence is < 1%. Amount of scattered radiation is about 10%. Energy threshold is 100 KeV.

*Detector pair resolution values are the average of the inherent detector pair resolutions from all 363 lines of response in the ECAT. The 1.6, 1.1 and 0.8 cm values are without and with the 2.3 and 1.5 cm wide shadow shields, respectively.

TABLE 3.

FRACTION OF TOTAL SYSTEM COUNTRATE DUE TO RANDOM COINCIDENCES*

Total System Countrate (counts/sec)	Random Coincidence / Total Coincidence (%)
50,000	17
20,000	8.0
10,000	4.1
5,000	2.1
1,000	0.7

*Phantom was 20 cm diam. x 5 cm long and contained a uniform distribution of $^{13}NH_3$ in water.

FIGURE CAPTIONS

Figure 1: Photographs of ECAT in Nuclear Medicine Clinic at UCLA.

Figure 2: Schematic illustration of typical scanning motions and example of fan beam geometry of multiple coincidence design of ECAT.

Figure 3: Illustration of the functional and interactive design of ECAT.

Figure 4: Line spread function (LSF) in ECT mode at high (HR), medium (MR) and low resolution (LR). Phantom was 20 cm in diam. with 2 mm diam. line sources separated by 1.4, 3.1, 4.8 and 6.5 cm from left to right. Histogram through images shows LSF's; each dot is separated by 2.5 mm. One standard deviation of resolution variance shown in image was calculated from resolved LSF's.

Figure 5: Measurement of ECAT linearity. Data were taken with a 20 cm diam. x 4 cm thick phantom containing $^{13}NH_3$. Solid line is the correct 10 min. half time of ^{13}N. Dots are measured countrates. Excellent linearity is observed over measured countrate.

Figure 6: Error estimate of ECAT. Reconstructed images of 20 cm diam. phantom containing uniform distribution of positron activity. Left:Medium resolution; Right: High resolution. Images contain 20 million counts. Experimental (exp) error (% S.D.) was calculated from center 15 cm diam. section as shown by region of interest in top image. Histogram profiles through center of images are shown. Theoretical (Theor) errors are calculated from eq. 1.

Figure 7: Reduction of motion artifacts due to redundant sampling scheme of ECAT. Top left: Sketch of phantom which is composed of outer cylinder with 19 cm diam., inner cylinder (off center) with 13.5 cm diam. and two small interior cylinders with 3 cm diam. Numbers in figure are relative activities. Top right:

Reconstructed image of phantom. Histogram profile at position of + signs on image are shown. Note that image values are in excellent agreement with activity values and small plastic wall which divides the left and right sides is seen even though its thickness is only 2 mm. Bottom left: reconstructed image with no motion. Bottom right: Reconstructed image in which phantom was moved in descrete 1.5 cm steps (ie, worse than continuous motion over same distance) 20 times in one direction during scan. Note that only minor artifacts appear. Resolution was medium and images contain about 7 million to provide high definition of possible artifacts.

Figure 8: Effect of redundant sampling and use of recalibration to reduce and remove errors due to possible detector instabilities. Top left: Reconstructed image with ECAT in calibration. Top right: Reconstructed image with 11 center coincidence lines of response (LOR) set to zero (disconnected). No significant artifacts are seen. Bottom left: 33 center LOR (11 on each bank) set to zero. Because of redundant sampling only modest artifacts are seen considering that 33 LOR are zero. Bottom right: ECAT was recalibrated with 33 LOR still set to zero and data reconstructed. Note artifacts seen in bottom left image are removed. Resolution was medium and images contain about 7 million counts to provide high definition of possible artifacts.

Figure 9: Left: Whole body rectilinear scan of human subject after inhalation of 10 mCi of ^{11}Co. Image shows general

blood distribution and prominant vessels and blood pools (ie, superior sagittal sinus, carotids, jugulars, heart chambers, spleen, iliacs, etc.). A-P and two ± 60° obliques are simultaneously recorded. Whole body transmission scan is also shown. Resolution was medium and total scan time for emission and transmission images were 40 min. each.

Figure 10: Whole body rectilinear scan of 19 Kg dog 90 min. after I.V. injection of 2.3 mCi of ^{18}FDG. Left: 40 min. emission scan. Center: 40 min. transmission scan. Right: Emission scan corrected for photon attenuation with data from center image. Resolution was medium.

Figure 11: Whole body rectilinear bone scan of 20 Kg dog one hour after injection of 3.5 mCi of ^{18}F. Resolution was medium and scan time was 40 min.

Figure 12: Left: Whole body rectilinear bone scan of patient with Hodgkins lymphoma two hours after injection of 5 mCi of ^{18}F. Resolution was medium resolution shadow shields - low resolution mode. Total scan time was 25 min. (see text for description). Right: 12 ECT scan from 4 cm above iliac crest in 15 mm steps down toward greater trochanter. There is good definition of the vertebral body, spinus process, iliac bones, ischiac bone, S.I. joint, sachrum, femur, etc. Arrows indicate lesions in iliac crest and head of femur. Resolution was medium, scan times were 3 min/level and images contain from 530,000 to 1.8 million counts.

Figure 13: Cerebral blood volume ECT images of human subject subsequent to single breath inhalation of 20 mCi of ^{11}Co. Images are from 4 cm above to 3.5 cm below (left to right) orbital meatal line. Images show blood distribution in the veins,

arteries and grey and white matter structures. Resolution was high (9.5 mm), images contain from 750 to 1.7 million counts and scan time was 4 to 5 min/level.

Figure 14: Example of interactive capability between rectilinear and ECT scans of ECAT. Left: transmission scans of thorax. Bottom: 3 min. limited field rectilinear scan showing use of joy stick (X is position of cursor) to select levels which are automatically carried out in ECT mode (shown above). Right: Emission images of thorax subsequent to inhalation of 10 mCi of ^{11}CO. Bottom: Shows 3 min. limited field rectilinear scan showing use of joy stick (X) to select levels which are then automatically studied with ECT as shown above. Emission images from top to bottom and left to right are from top of heart in 15 mm steps toward apex. First image shows right ventricle and out flow tract, right atrium, pulmonary artery, left ventricle, left atrium and aorta. Second image shows right ventricle, superior venacava, left ventricle, left out-flow and aorta. Third and fourth images show right ventricle and aorta. Septum is well visualized. Fifth and sixth levels show left and right ventricle, inferior venacava, right atrium and aorta. Inner ventricular septum is well defined. Images are ungated, resolution was medium and images contain from 600,000 to 3 million/level. Scan times were 7 mins./level.

Figure 15: ECT images of myocardial glucose metabolism in human subject 30 min. after I.V. injection 4.6 mCi of ^{18}FDG. Scan times were 7 min/level and images contain from 350,000 to 600,000 counts. Resolution was medium and images are ungated. Major structure seen is left ventricle. Right ventricle is seen in top image. Images are from top to apex of heart in 18 mm steps.

Figure 16: Selected ECT images of cerebral "perfusion" and glucose metabolism subsequent to I.V. injection of $^{13}NH_3$ (20 mCi) and ^{18}FDG (5 mCi), respectively. Images contain from 700,000 to 2 million counts/level. Scan times for $^{13}NH_3$ were 3 min/level and 7 min/level with ^{18}FDG. Note delineation of superficial cortex, visual cortex, left and right internal grey nuclei in region of basal ganglia and internal capsule. Photographs of brain slices are shown at left for anatomical comparisons. $^{13}NH_3$ and ^{18}FDG scans are from different subjects and therefore levels are not exactly comparable. Resolution was medium.

Figure 17: Selected images from patient with right occipital infarct. $^{13}NH_3$ and ^{68}GaEDTA images show perfusion and blood brain barrier (NNN) defect. High level of activity seen in center - posterior region is blood activity in superior sagittal sinus. Note that if $^{13}NH_3$ images are superimposed on ^{68}GaEDTA the BBB defect corresponds directly to perfusion defect. Brain slices (not same patient) are shown for anatomical comparison. X-ray CT scans with and without radiographic contrast material were negative. Resolution was medium.

Figure 18: Selected images from $^{13}NH_3$, $^{68}GaEDTA$ and x-ray CT scan (with contrast) of patient with a glioblastoma. Resolution was medium. See text for discussion of images.

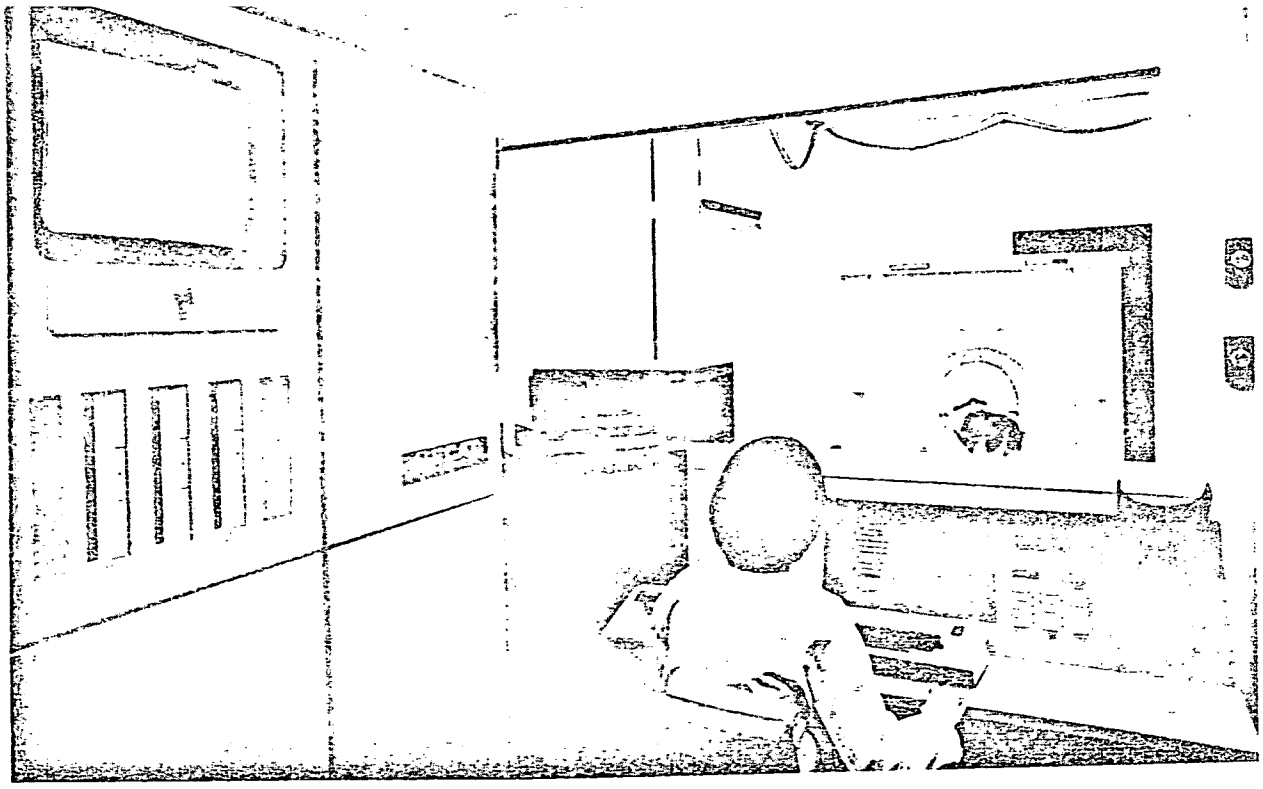

FIGURE 1.

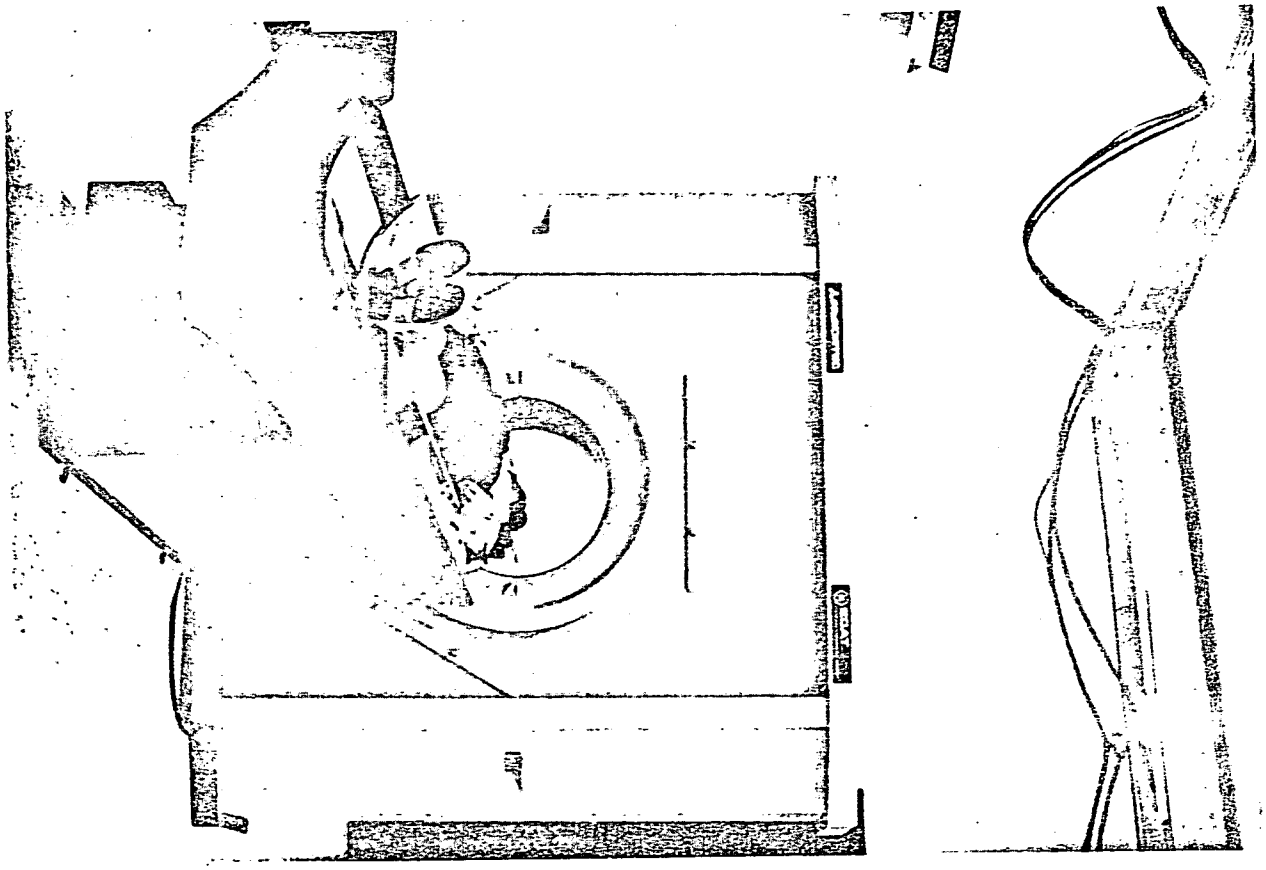

FIGURE 1a.

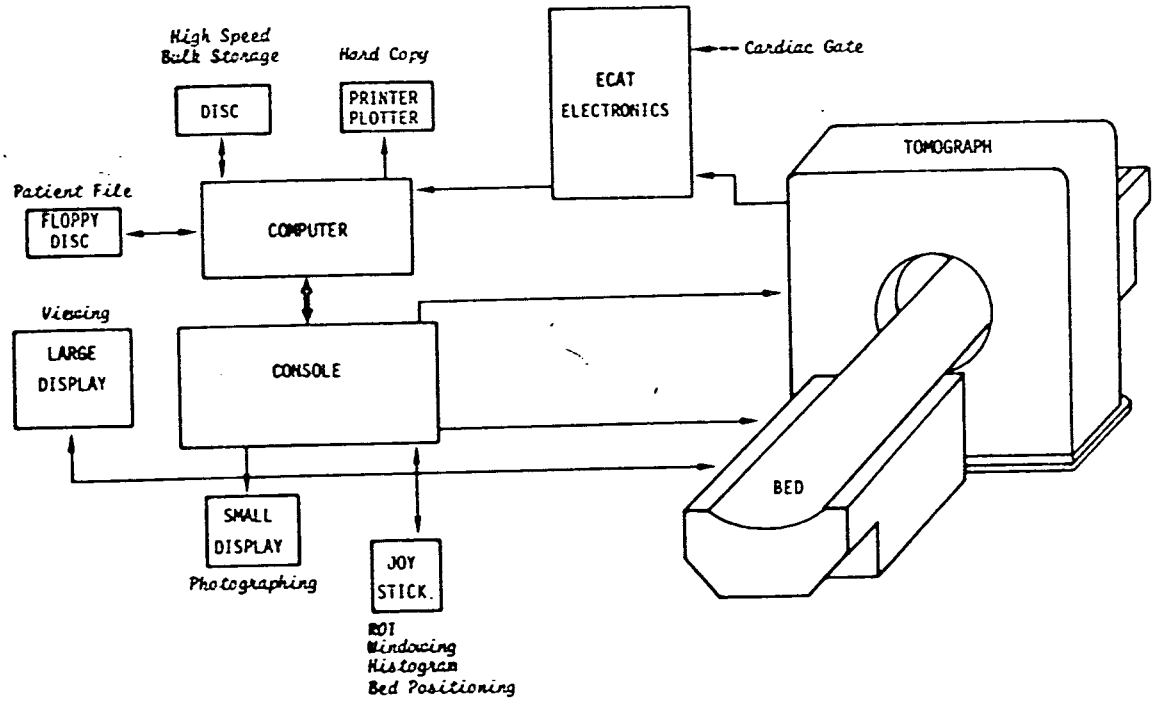

FIGURE 2.

FIGURE 3.

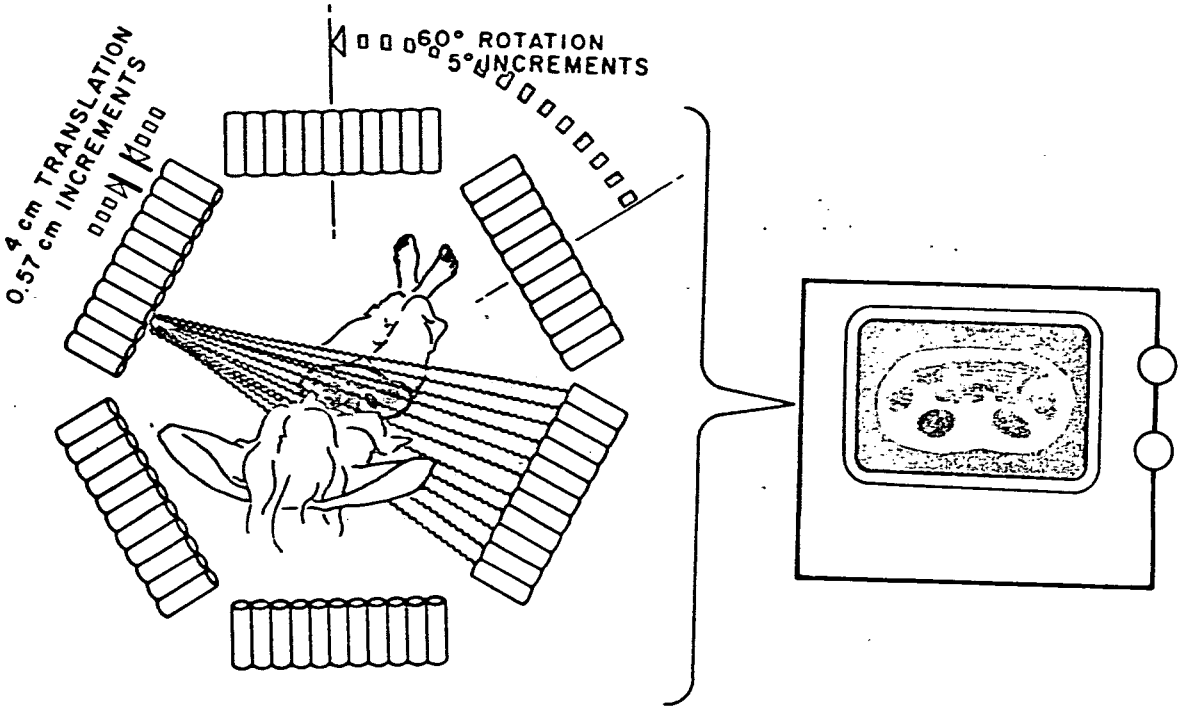

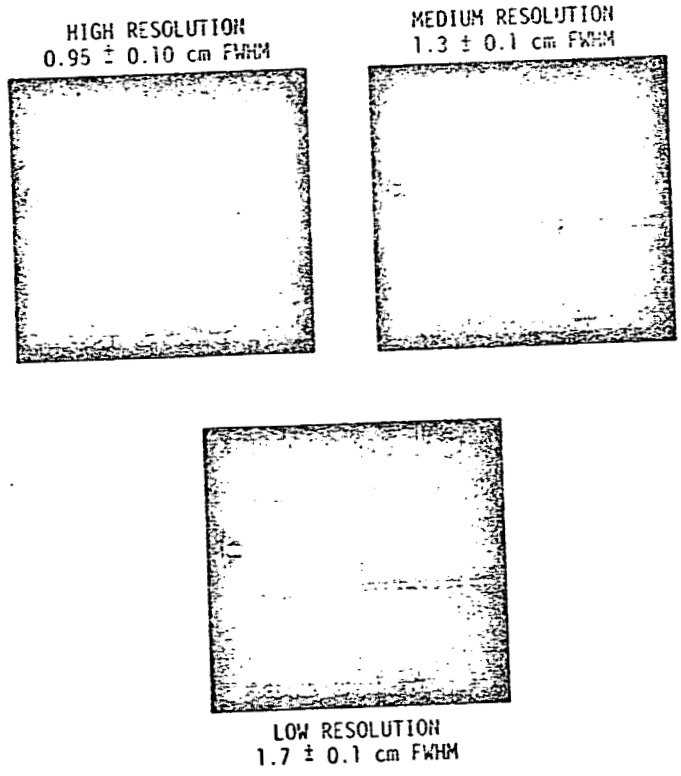

FIGURE 4.

FIGURE 5.

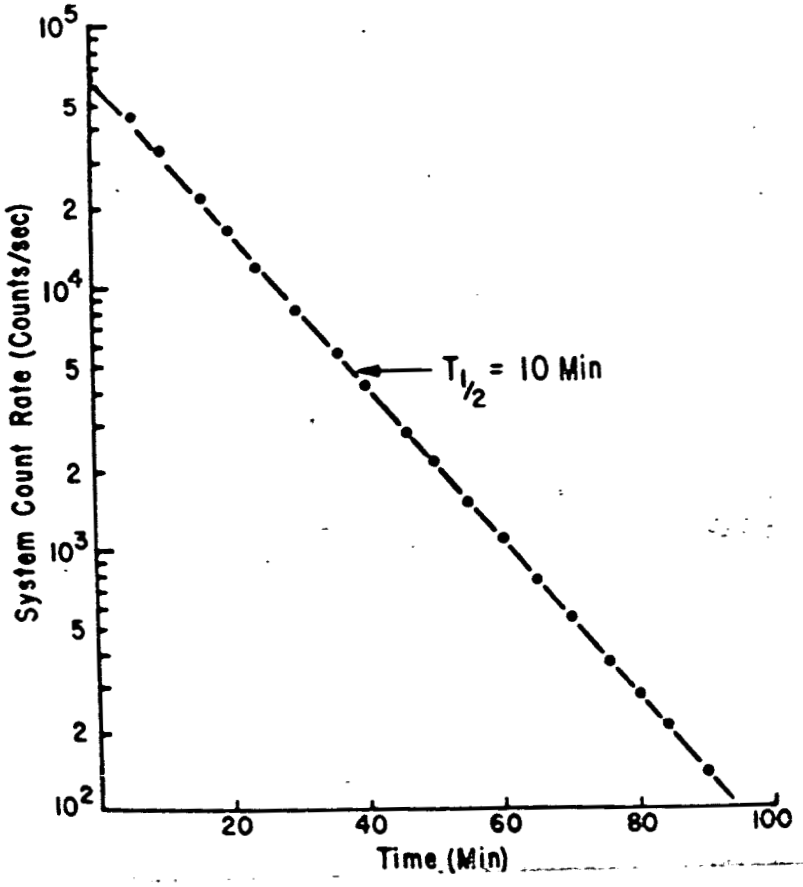

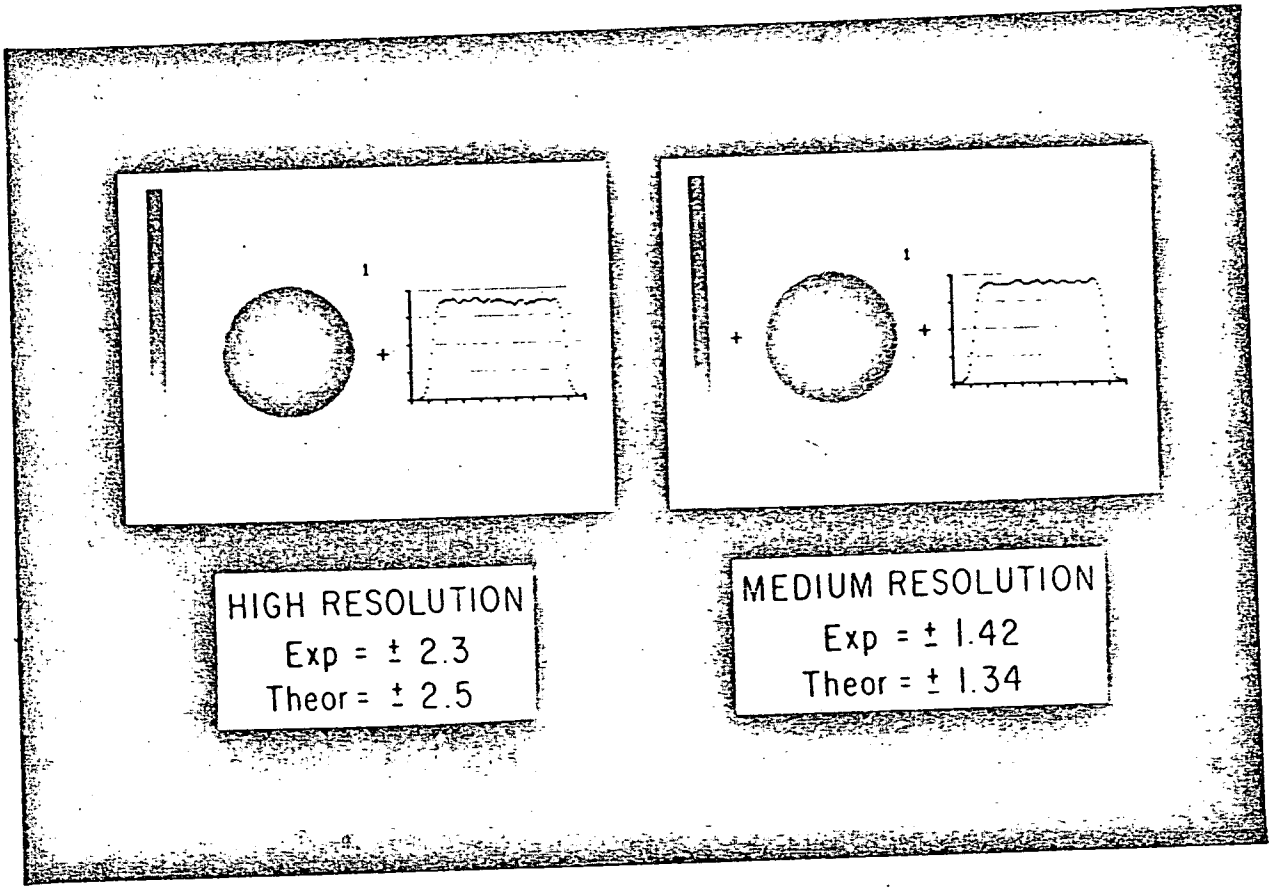

FIGURE 6.

FIGURE 7.

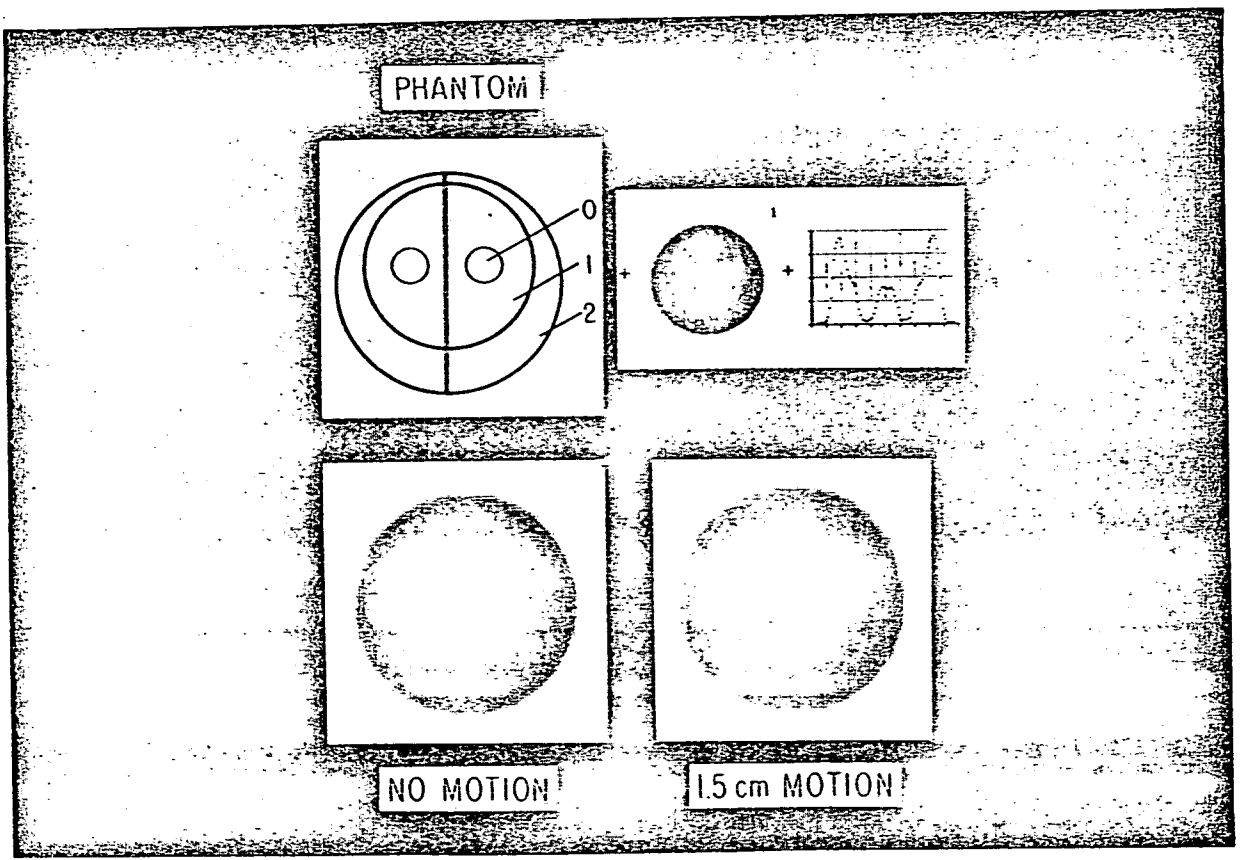

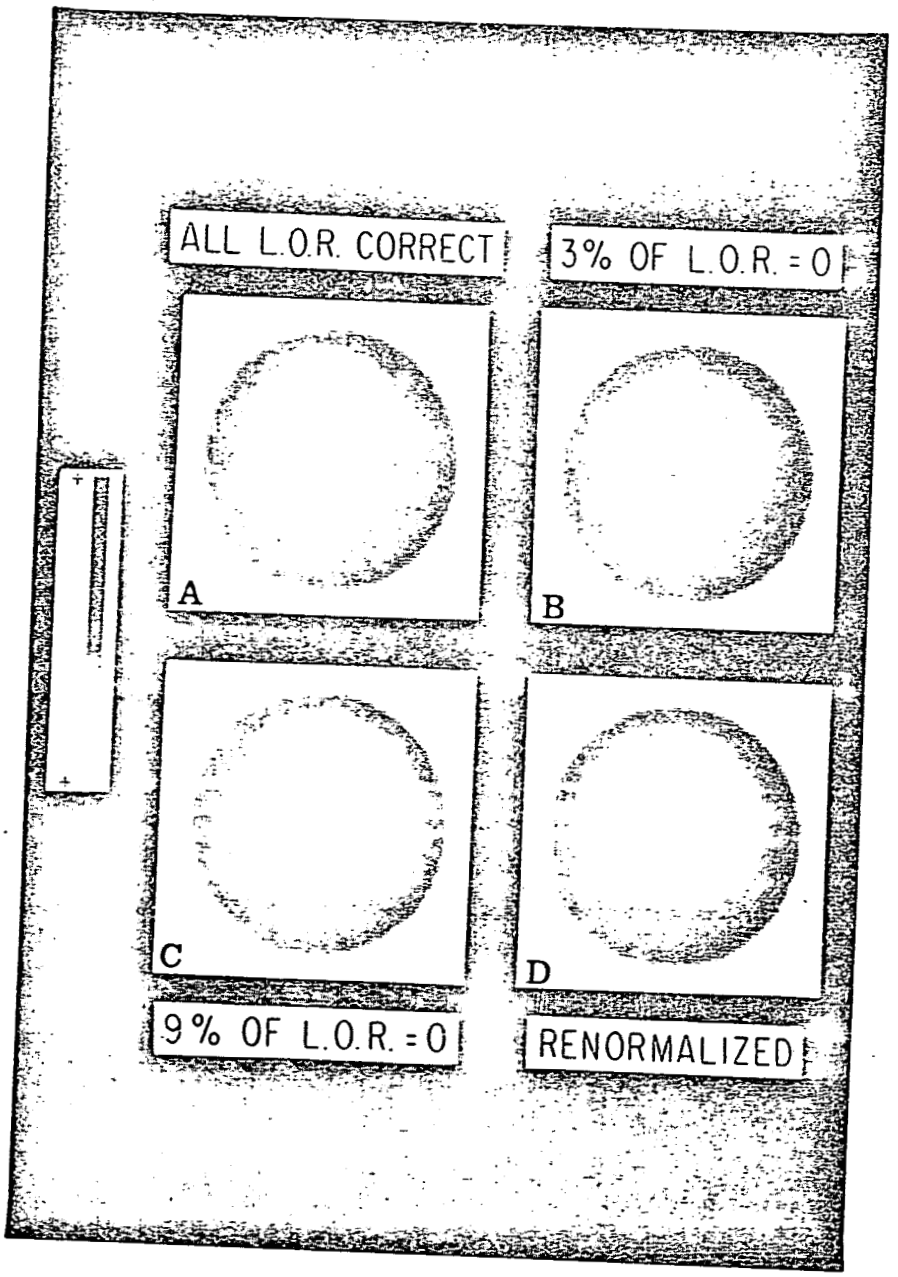

FIGURE 8.

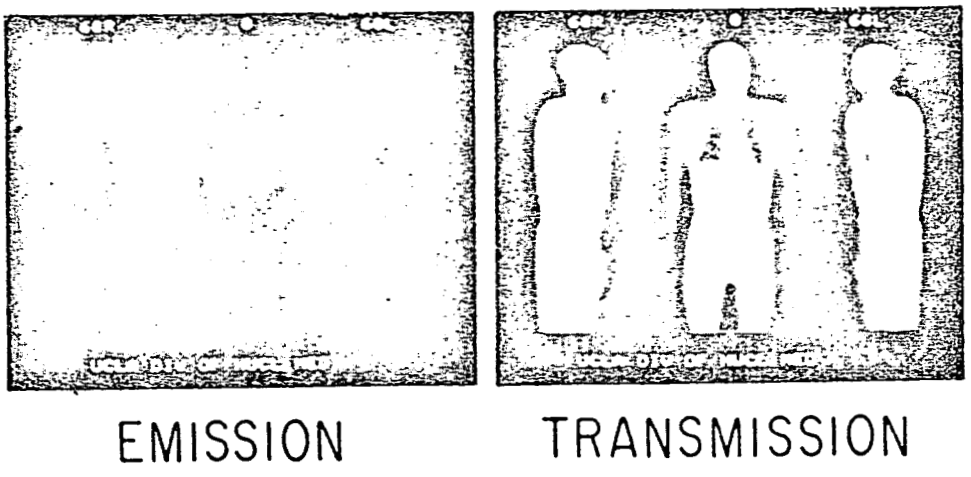

FIGURE 9.

FIGURE 10.

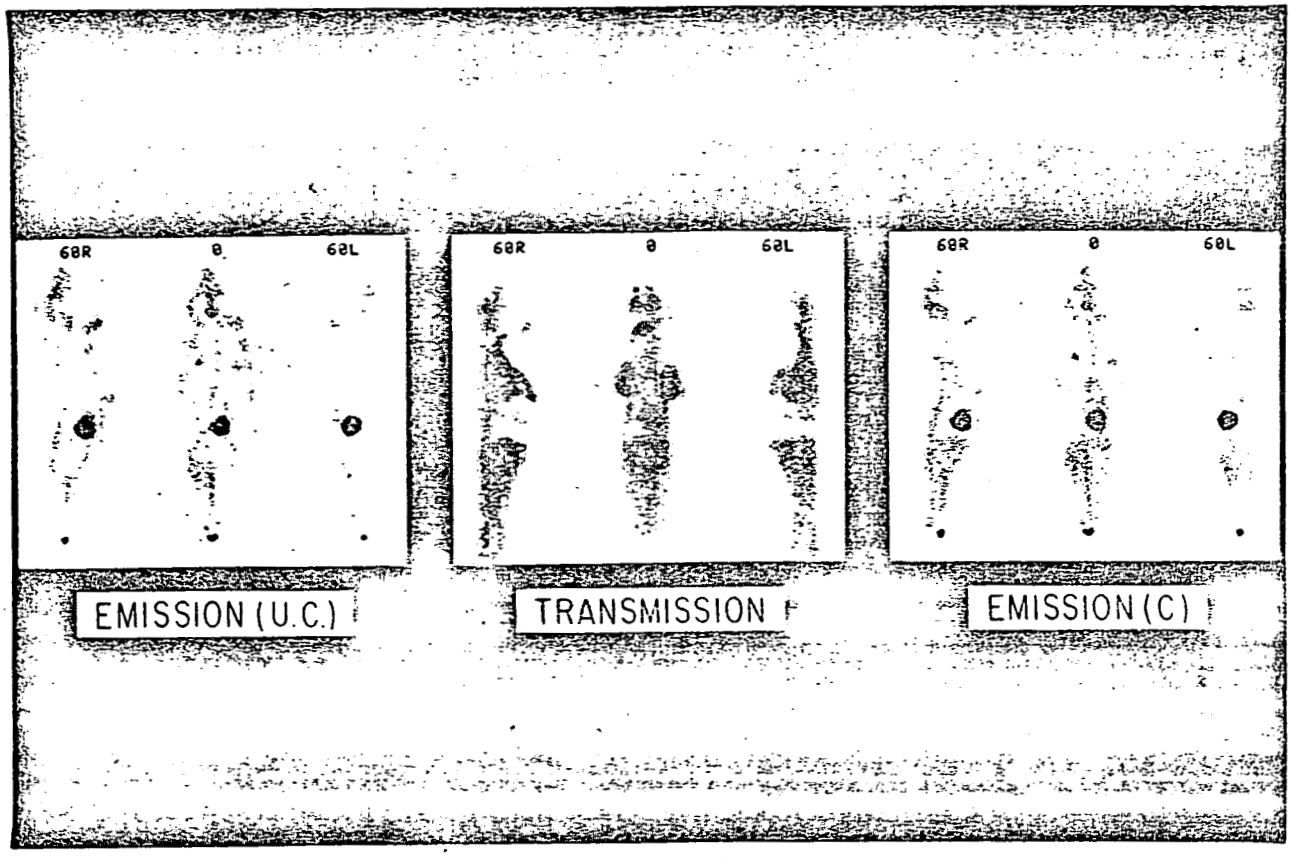

RECTILINEAR SCANS (DOG)

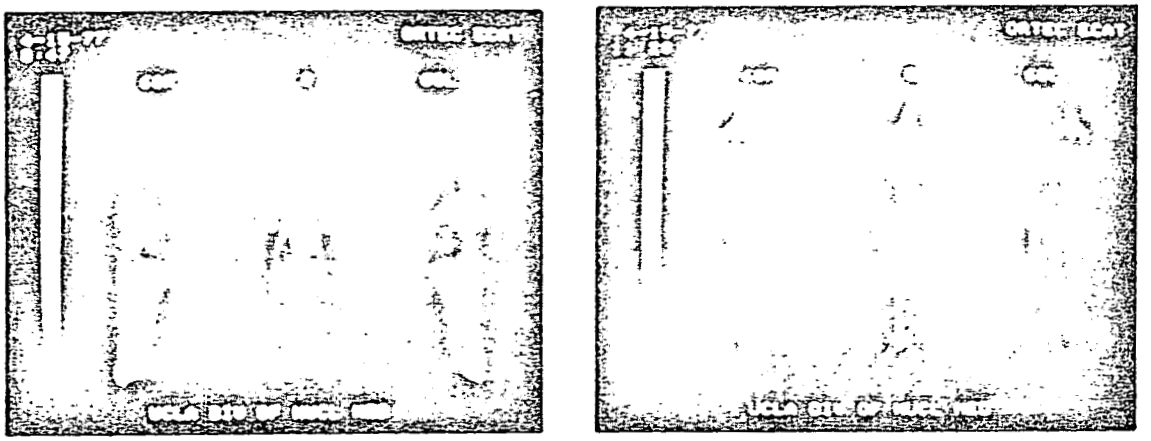

TRANSMISSION ^{18}F - EMISSION

FIGURE 11.

FIGURE 12.

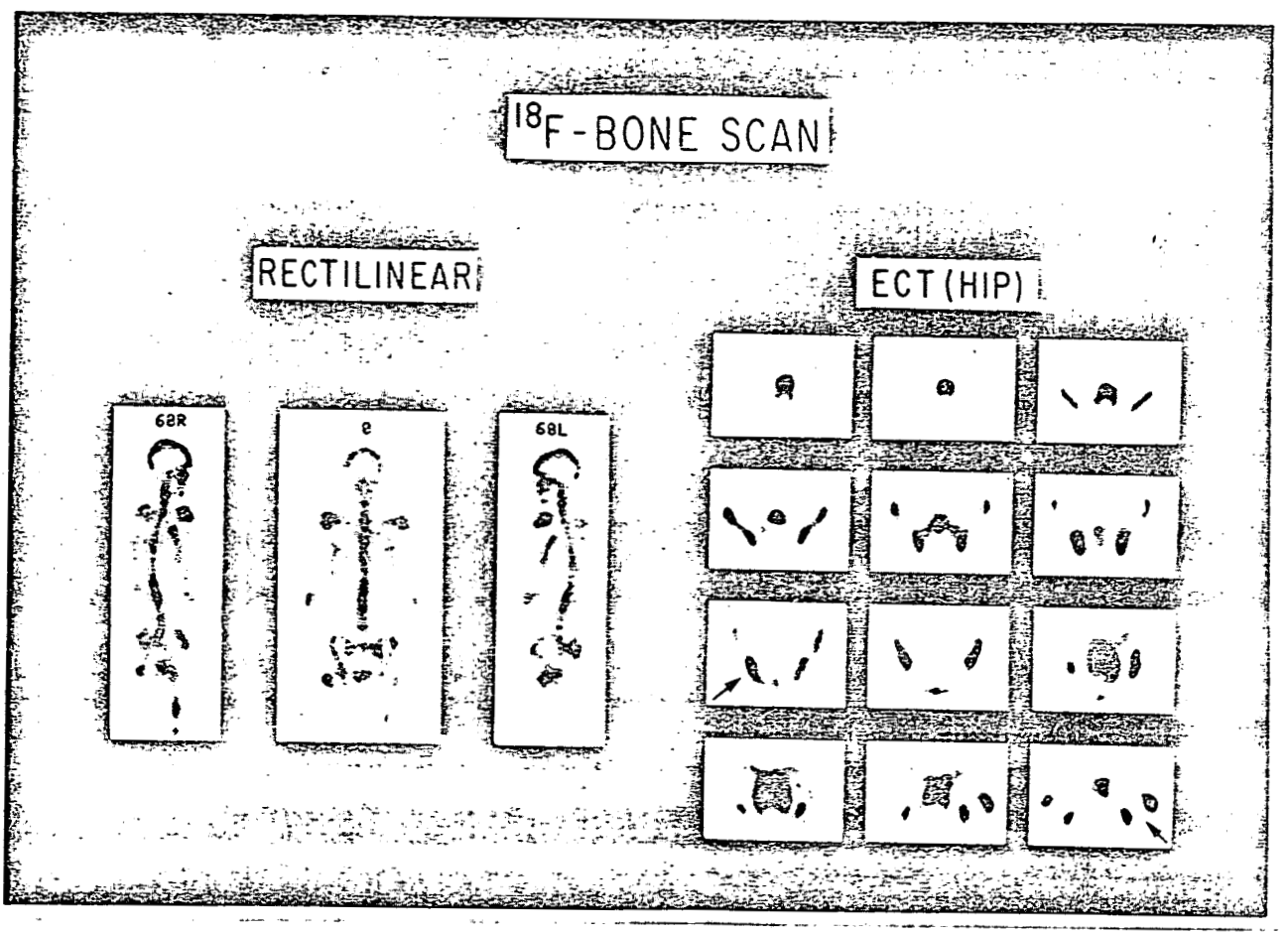

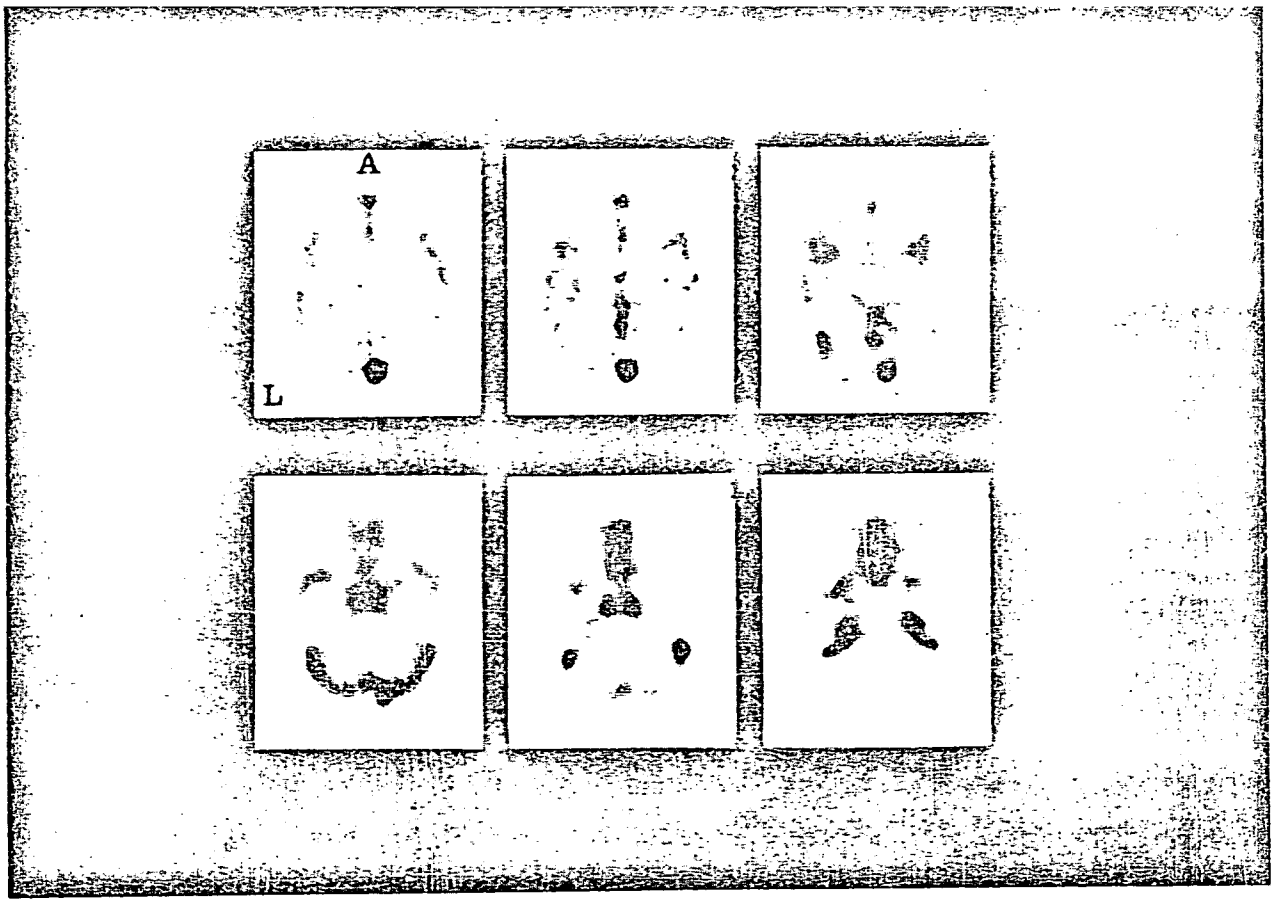

FIGURE 13.

FIGURE 14.

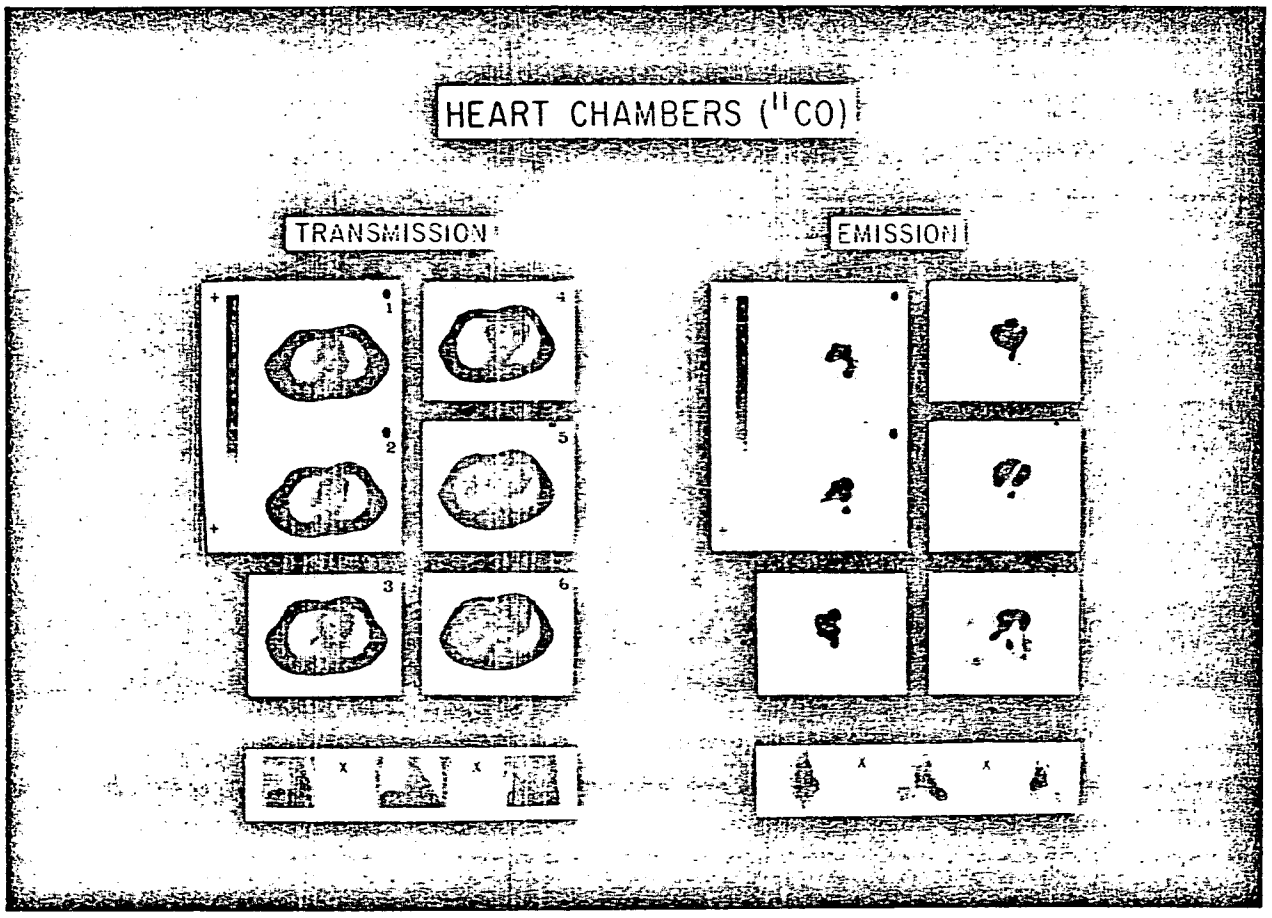

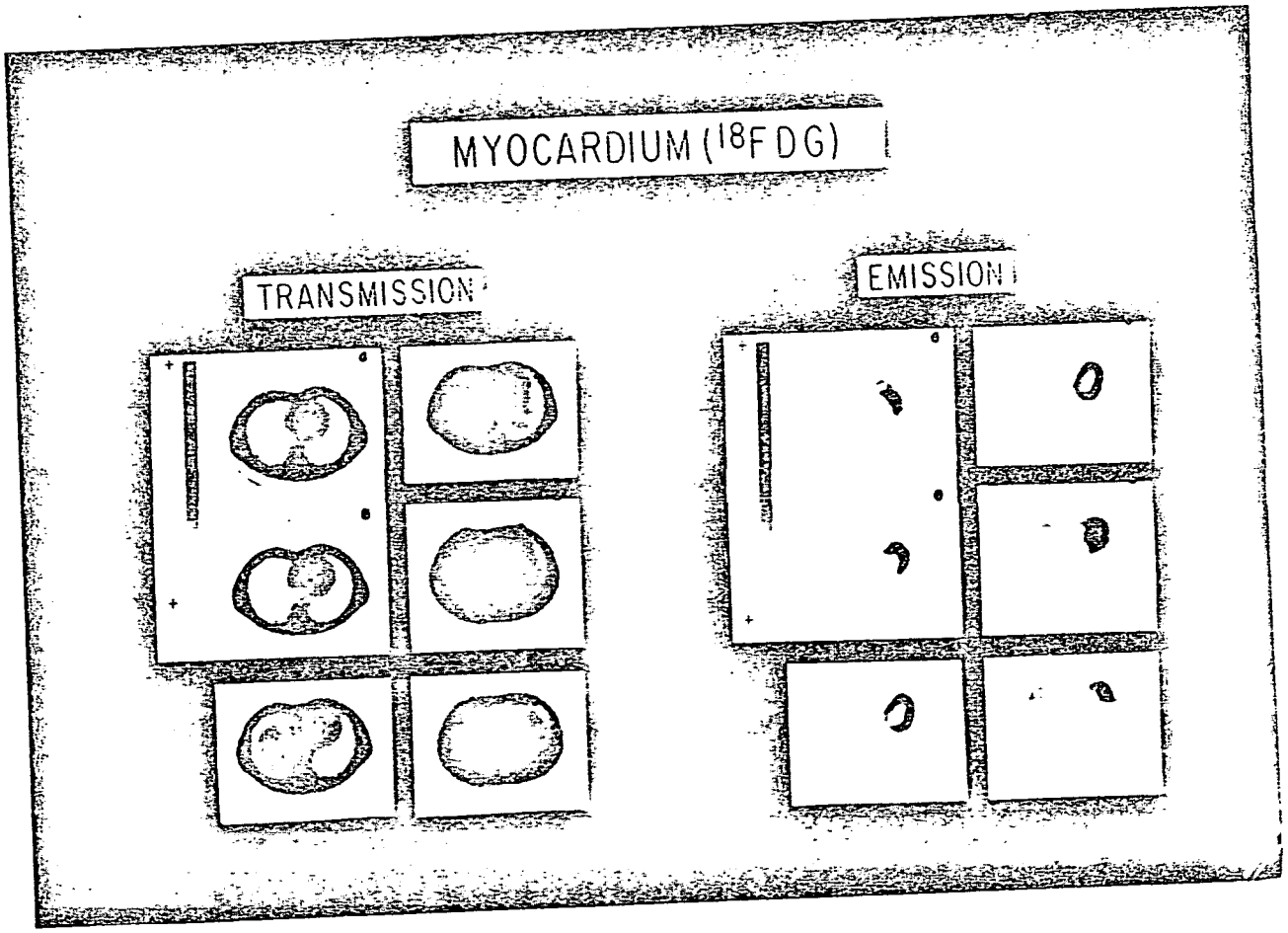

FIGURE 15.

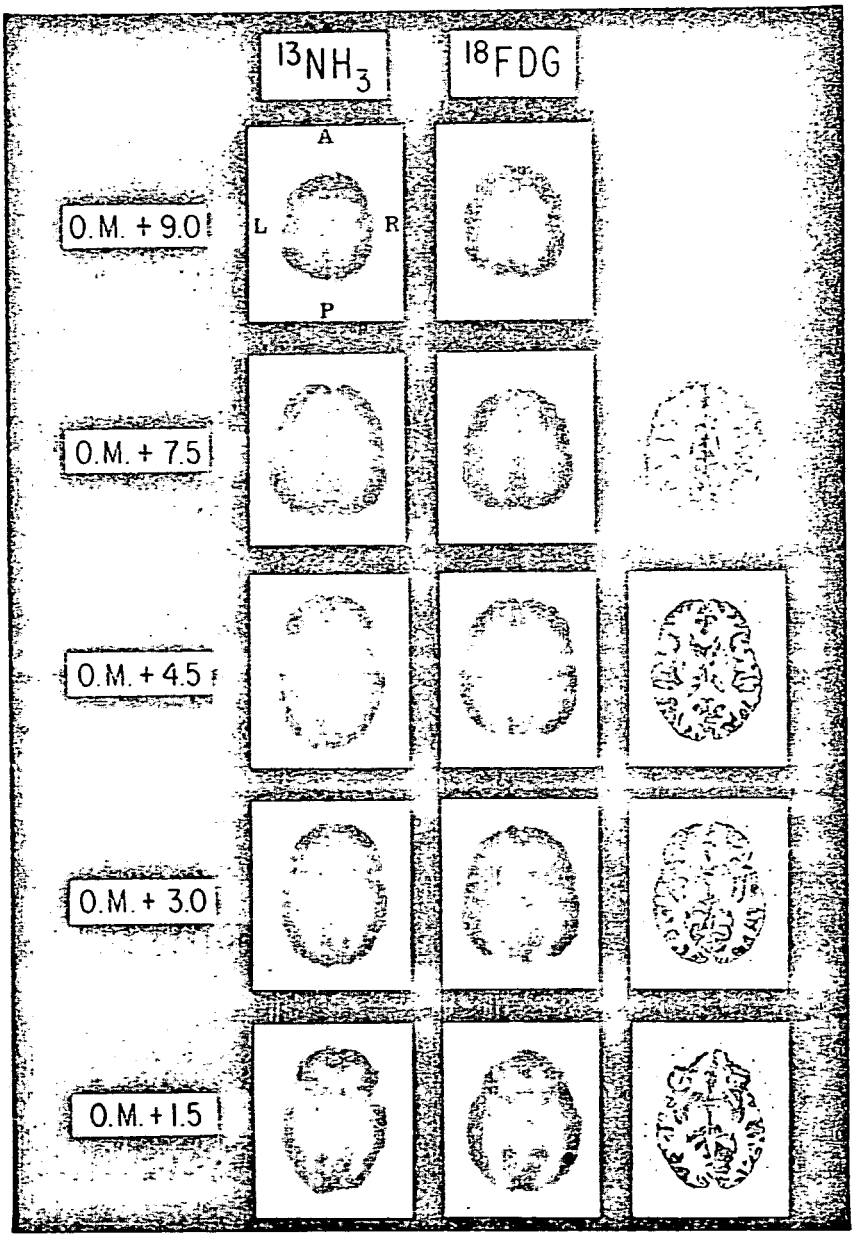

FIGURE 16.

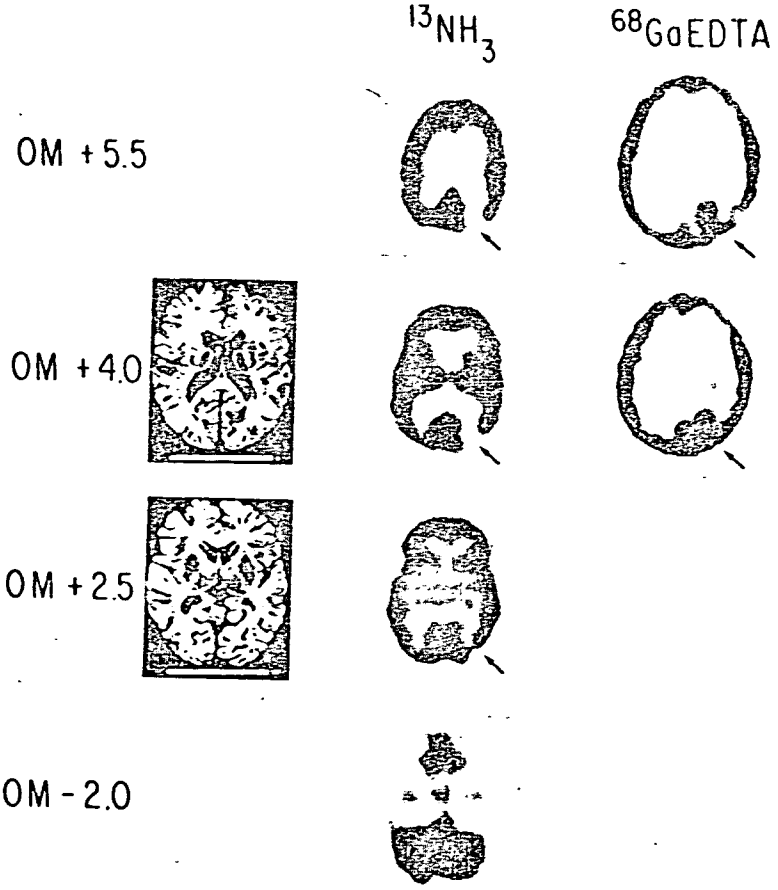

FIGURE 17.

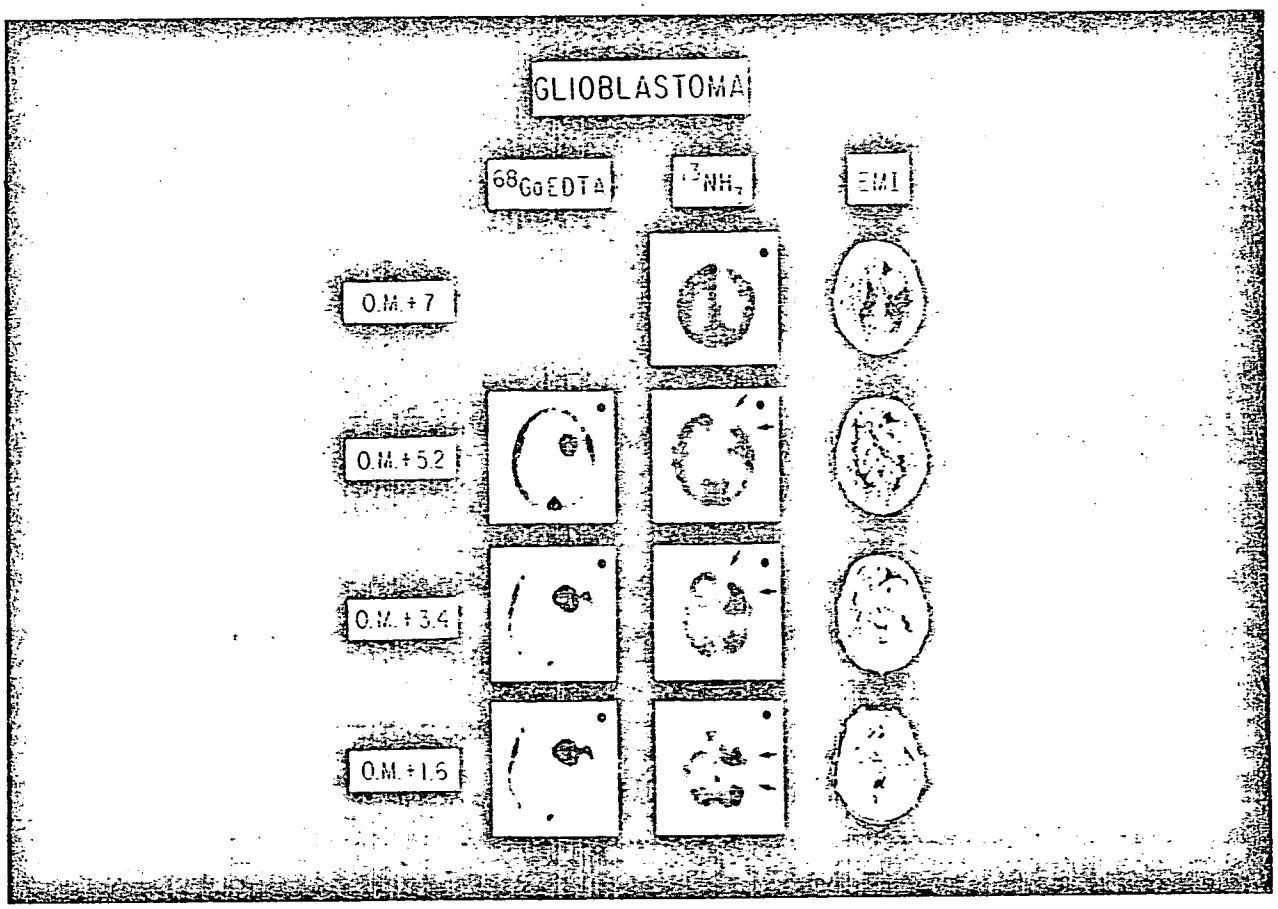

FIGURE 18.